J. Appl. Comput. Mech., 12(3) (2026) 1256-1275
DOI: 10.22055/jacm.2026.48955.5622

ISSN: 2383-4536
jacm.scu.ac.ir

Shahid Chamran University of Ahvaz

Journal of
Applied and Computational Mechanics

Research Paper

Bulging and Bending of a Thick-Walled Cylinder with Residual Stress under Combined Extension and Inflation

Murtadha J. Al-Chlaihawi[1], Alejandro Font[2], Heiko Topol[3], Hasan Demirkoparan[4], José Merodio[5]

[1]Civil Engineering Department, University of Al-Qadisiyah, 58001 Al-Qadisiyah, Iraq, Email: murtadha.hussein@alumnos.upm.es

[2]Programa de Ing. Estructural, Cimentaciones y sus Materiales, E.T.S. Ingenieros Caminos, Canales y Puertos, Universidad Politecnica de Madrid, Madrid, Spain, Email: ad.font@alumnos.upm.es

[3]Department of Mechanical Engineering, New Uzbekistan University, Movarounnahr Street 1, Tashkent, 100007, Uzbekistan, Email: h.topol@newuu.uz

[4]Carnegie Mellon University in Qatar, Education City, P.O. Box 24866, Doha, Qatar, Email: hasand@andrew.cmu.edu

[5]Departamento de Matemática Aplicada a las TIC, ETS de Ingeniería de Sistemas Informáticos, Universidad Politecnica de Madrid, 28031, Madrid, Spain, Email: jose.merodio@upm.es

Received November 30 2025; Revised April 12 2026; Accepted for publication April 13 2026.
Corresponding author: Heiko Topol (h.topol@newuu.uz)

Abstract. Bifurcation is a localized instability that has been extensively studied. However, this sort of instability was not given sufficient consideration in the presence of residual stresses, particularly generalized non-planar residual stresses. This study aims to investigate the bifurcation phenomena in hyperelastic materials subjected to generalized residual stresses. Residual stresses predominantly arise in arterial wall tissue due to various factors, including growth and development. These residual stresses influence the mechanical response of hyperelastic materials and play a crucial role in the locus of the bulge along a bifurcating cylindrical tube. In this paper, the impact of the mechanical behavior and residual stresses on bifurcation instability with application to aneurysms is investigated. The analysis employs numerical simulations grounded in a proposed methodology integrated into the finite element code through a user-defined material subroutine. The finite element modeling utilizes the commercial software ABAQUS and applies the modified Riks method. The results show that bending is the initial bifurcation mode for relatively small axial stretches, while at higher stretches the (pure) bulging mode is more likely, serving as the lower bound. For small stretches, if bending is prevented, the bulging that occurs requires higher internal pressures than when bending is allowed, indicating that avoiding bending may delay aneurysm formation. Post-bending bulges developing sideways in the studied cylinders resemble abdominal aortic aneurysms, whereas balloon-shaped bulges in (pure) bulging modes are associated with arterial rupture.

Keywords: Three-dimensional residual stress, Abdominal Aortic Aneurysms (AAA), Bulging bifurcation, Bending bifurcation, Finite element method.

1. Introduction

Aneurysms consist of abnormal localized bulges that occur in blood vessels and are related to various biomechanical factors such as cell degradation, age, hypertension, heterogeneity of the material, biochemical reactions, and anisotropy. Abdominal aortic aneurysms have been reported to be involved in a significant number of deaths in developed nations [1], and arterial wall rupture has a high mortality rate [2]. Changes in the mechanical pattern of collagen fibers can lead to aneurysm or bulging bifurcation [3].

Hyperelastic materials have received substantial attention in biomedical engineering research, particularly the mechanical response of hollow tubes subjected to residual stresses in the context of aneurysms [4–7]. This field has considerable potential to advance our understanding of the biomechanical complexities associated with aneurysms and pathological dilation of blood vessel walls, which pose significant health risks due to their propensity to rupture [8]. Understanding the mechanics underlying the initiation, progression, and rupture of aneurysms is essential for the development of effective diagnostic and therapeutic strategies [9].

Residual stresses within the arterial wall tissue, which result from developmental processes and hemodynamic loading, significantly influence the biomechanical behavior of aneurysms [10]. The intricate interaction between material properties, geometric configurations, and residual stresses fundamentally determines the mechanical response of these materials under various loading conditions [11]. Through the application of advanced computational modeling techniques, such as finite element analysis (FEA), researchers can simulate and evaluate the deformation patterns and stress distributions within hyperelastic tubes subjected to three-dimensional residual stresses [12]. Furthermore, recent advances in computational modeling methodologies enable the development of novel design approaches to predict the mechanical behavior of these materials [13].

Few studies have specifically addressed bifurcation phenomena in arterial wall tissue in the presence of initial stresses. However, remarkable works have been performed to study this type of instability, for example, a cylindrical tube inflated under swelling effects [14–16]. In addition, inflation and propagation of aneurysms in human arterial wall tissue with a residual stress field have been investigated in the context of bifurcation [3, 17–23]. The weakening of the arterial wall may be affected by degradation of collagen and elastin (two proteins that provide strength and elasticity to the arterial wall), for example, due to enzymatic activity in the tissue [24–26].

Published online April 15 2026

Many researchers have made great efforts in the form of experimental, analytical, and numerical work to provide solutions to the problem at hand. Experimental studies, such as those of [5, 27–30], have provided insight into the mechanical properties of different materials and their response to various loading conditions. However, there is a limited amount of existing experimental data that covers all the parameters that affect this particular problem. The work of [31–35] provides a comprehensive theoretical framework to include the modeling of residual stresses in hyperelastic materials, laying the essential foundation for future research in this area. While applicable for relatively simple cases, the theoretical approach cannot handle highly non-linear conditions, and one needs to find alternatives to solve problems in which one of the purposes is the post-critical behavior. Computational modeling efforts, such as finite element analysis (FEA) simulations conducted in [17, 19, 20, 36, 37], for example, have played an important role in explaining the complex interaction between material properties, geometric configurations, and residual stress distributions in hyperelastic materials. These studies have advanced our understanding by quantifying the influence of residual stresses on the mechanical behavior of hyperelastic materials under various loading conditions, offering valuable predictive capabilities for biomedical applications, including aneurysm biomechanics. Residual stresses occur in the unloaded state of arterial wall tissue and generally arise from many factors, specifically growth and development [38]. These initial stresses can affect arterial wall tissue, causing cardiovascular diseases such as aneurysm formation. Understanding residual stresses and their distribution can provide success in the analysis and design process of many engineering applications, such as the problem under consideration. The introduction of residual stresses has been presented in [39–42]. Residual stresses in two dimensions have been applied for the study of bulging (axisymmetric) and bending (asymmetric) bifurcations in [19, 20].

Significant research has been developed on the mechanical response of biological systems with a particular focus on arterial wall tissue in relation to bifurcation phenomena; however, research and advances concerning hollow tubes composed of hyperelastic materials under residual stresses remain relatively sparse, especially in cases involving non-planar residual stresses. Important work on such initial stresses has been conducted in the context of aneurysm in arterial wall tissue [36] and with emphasis on the human aorta [43,44]. The current study presents a comprehensive perspective on the implementation of three-dimensional residual stresses and examines the impact of these stresses and their distribution on the material's behavior under investigation. The efforts have been dedicated to developing an appropriate methodology where bifurcation and post-bifurcation for cylinders under extension and inflation with residual stresses can be captured using numerical analyses. These approaches are developed by employing finite element analysis using the Modified Riks Method, which is a built-in approach from commercial software ABAQUS [45]. The material model has been implemented through the subroutine UMAT.

Building upon the foundations laid by these studies, this research aims to further investigate the mechanical behavior of hollow tubes composed of hyperelastic materials under the influence of three-dimensional residual stresses, with a specific focus on their application to aneurysm biomechanics. By deriving a constitutive model based on the strain energy function, this study aims to explain the intricate interplay between material properties, geometric configurations, and generalized residual stresses, with the ultimate goal of proposing a methodology and incorporating this methodology into the finite element code of ABAQUS to become an informative framework that can be adopted in comparable problems.

The paper is arranged as follows. A mathematical description of the problem at hand is presented in Section 2. The constitutive equation based on the strain energy function is introduced to model human artery wall tissue through an incompressible hyperelastic material. In Section 3, a numerical technique to model extended and inflated circular cylindrical tubes subjected to residual stress is offered. The numerical results and analysis are discussed and illustrated graphically in Section 4. Three possible modes of bifurcation for the above-mentioned numerical results are distinguished, namely, prismatic, bulging (axisymmetric), and bending (asymmetric) modes, but, in this paper, the focus is on the last two modes, which are investigated in detail and compared with each other. Finally, in Section 5, a conclusion is drawn based on the analysis of the results obtained.

2. Mathematical Description of the Problem

2.1 Geometry

In a reference configuration $\mathcal{B}_r$, consider a tube with inner radius A, outer radius B, and length L. In terms of cylindrical coordinates (R, Θ, Z), the geometry of the cylinder can be described as

$$A \leq R \leq B, \quad 0 \leq \Theta \leq 2\pi, \quad 0 \leq Z \leq L. \tag{1}$$

Assume that the cylinder subjected to both inflation due to an inner pressurization and an applied axial stretch maintains its circular cylindrical shape. The location of a material point in the cylinder in the reference configuration $\mathcal{B}_r$ is described by the position vector $\mathbf{X}$. In the deformed configuration $\mathcal{B}$, the position vector $\mathbf{x}$ indicates the location of any point in the cylinder wall. The deformed configuration and the reference one are related via the deformation gradient tensor $\mathbf{F} = \partial\mathbf{x}/\partial\mathbf{X}$.

Under these circumstances, the deformation gradient tensor $\mathbf{F}$ can be expressed in terms of the three principal stretches in the cylinder wall: the radial stretch λ_r, the azimuthal stretch $\lambda_\theta = r/R > 0$, and the axial stretch $\lambda_z = z/Z$, where (r, θ, z) are cylindrical coordinates in the deformed configuration, and length ℓ is the length of deformed tube. Hence, one can write

$$\mathbf{F} = \text{diag}(\lambda_r, \lambda_\theta, \lambda_z). \tag{2}$$

The determinant of the deformation gradient tensor gives the ratio of the material volume in the current or deformed configuration $\mathcal{B}$ to the material volume in the reference configuration $\mathcal{B}_r$. The consideration of material volume changes is applicable when, for instance, swelling or deswelling effects are included, which are often linked to different diseases. The relationship between intima-media thickness (IMT), various risk factors, and cardiovascular diseases has been examined by O'Leary & Polak [46] and Polak et al. [47]. Swelling effects in incompressible hyperelastic solids are considered in various modeling works (see, e.g, Al Chlaihawi et al. [14], Gou et al. [48], Moradalizadeh et al. [49], Topol et al. [15, 16], and Nazari et al. [50]).

In the framework of this article, the material is taken to be incompressible for which the determinant of the deformation gradient tensor becomes equal to one,

$$\det\mathbf{F} = 1. \tag{3}$$

As the volume of material remains constant due to its incompressible nature, the incompressibility constraint (3) can be used to express the radial stretch in terms of the other two stretches

$$\lambda_r = \lambda_\theta^{-1}\lambda_z^{-1}. \tag{4}$$

Equation (3) only allows volume-preserving (isochoric) deformations. The deformation is often described using the right Cauchy-Green deformation tensor $\mathbf{C} = \mathbf{F}^{\mathbf{T}}\mathbf{F}$. The displacement $\mathbf{u}$ of a material point is $\mathbf{u} = \mathbf{x} - \mathbf{X}$.

2.2 Residually stressed cylinders

As the arterial wall grows and alters in response to its mechanical environment, it suffers from a series of irreversible processes. Residual stress has to be taken into account in the material model. In the absence of body forces, the Cauchy stress tensor $\boldsymbol{\sigma}$ and the nominal stress tensor $\mathbf{S}$ satisfy

$$\mathrm{div}\boldsymbol{\sigma} = \mathbf{0}, \quad \mathrm{Div}\mathbf{S} = \mathbf{0}, \tag{5}$$

respectively, where the divergence operator div is related to the current configuration, while Div is related to the reference configuration.

In this article, it is assumed that the body is initially subjected to residual stress given by a second-order tensor $\boldsymbol{\sigma}_0$, which exists in the absence of body forces and surface traction on the boundary of the solid in $\mathcal{B}_\mathrm{r}$ (see [39]). As residual stress is defined in the reference configuration $\mathcal{B}_r$ and is assumed to be unaffected by rotations in the deformed configuration $\mathcal{B}$, the residual stress tensor is inherently objective [41].

Due to the absence of traction on the surface, the residual stress tensor fulfills the condition

$$\sigma_0 \mathbf{N} = \mathbf{0} \qquad \text{on} \qquad \partial\mathcal{B}_\mathrm{r}, \tag{6}$$

where $\mathbf{N}$ is an outward normal unit vector and $\partial\mathcal{B}_r$ is the boundary of $\mathcal{B}_\mathrm{r}$. The residual stress tensor is symmetric $\boldsymbol{\sigma}_0^\mathrm{T} = \boldsymbol{\sigma}_0$, and satisfies the equilibrium equation

$$\mathrm{Div}\boldsymbol{\sigma}_0 = \mathbf{0}. \tag{7}$$

Several approaches have been proposed to account for residual stresses in the mechanical modeling. Different works apply different natural configurations of the constituents, and a deformation-gradient-like tensor is introduced for the mapping of these natural configurations; for instance, Topol et al. [51, 52] and Gou et al. [48] consider pre-stretched fibers that tend to contract the fiber-embedding isotropic ground material. One widely used technique is the *opening angle method*, which assumes that a sector cut from a cylinder represents its stress-free configuration. When the sector is closed to restore the cylindrical shape, residual stresses naturally arise in the material. This approach offers a direct connection between the modeling of residual stresses and experimental observations, and it has been applied in numerous studies [50, 53–57]. An alternative strategy introduces residual stresses through residual stress tensors. In this case, the strain energy density function is expressed in terms of invariants constructed from these tensors. This framework has been employed in a variety of works [41, 42, 58–60] and, more recently, adapted for finite element analyses relevant to arterial tissue [19, 20, 23, 36, 61].

The works [17, 19, 20, 44] deal with the modeling of cylinders in which the residual stress tensor only affects the planar sections, meaning that the initial formulation has only non-zero values for the components $\sigma_{0\mathrm{RR}}$ and $\sigma_{0\Theta\Theta}$, in [36] that earlier approach is generalized.

In the following, we apply an ansatz for the three-dimensional residual stress distribution that has been presented by Al-Chlaihawi et al. [23]:

$$\sigma_{0\mathrm{RR}} = \alpha_\mathrm{c}(\mathrm{R} - A)(\mathrm{R} - B), \tag{8}$$

$$\sigma_{0\mathrm{R}\Theta} = 0, \tag{9}$$

$$\sigma_{0\mathrm{RZ}} = \frac{\alpha_\mathrm{d}}{\mathrm{R}}\left[(\mathrm{R} - A)(\mathrm{R} - B)(5\mathrm{Z}^4 - 9\mathrm{Z}^2\mathrm{L}^2 + 4\mathrm{Z}\mathrm{L}^3)\right], \tag{10}$$

$$\begin{aligned}\sigma_{0\Theta\Theta} = {} & \alpha_\mathrm{c}\left[(\mathrm{R} - A)(\mathrm{R} - B) + \mathrm{R}(\mathrm{R} - A) + \mathrm{R}(\mathrm{R} - B)\right] \\ & + \alpha_\mathrm{d}\left[(\mathrm{R} - A)(\mathrm{R} - B)(20\mathrm{Z}^3 - 18\mathrm{Z}\mathrm{L}^2 + 4\mathrm{L}^3)\right],\end{aligned} \tag{11}$$

$$\sigma_{0\Theta\mathrm{Z}} = 0, \tag{12}$$

$$\sigma_{0\mathrm{ZZ}} = -\frac{\alpha_\mathrm{d}}{\mathrm{R}}\left[(2\mathrm{R} - A - B)(\mathrm{Z}^2)\,(\mathrm{Z}^3 - 3\mathrm{Z}\mathrm{L}^2 + 2\mathrm{L}^3)\right]. \tag{13}$$

which satisfies the conditions to be considered a residual stress tensor (i.e., it satisfies (6) and (7)), and where α_c and α_d are (residual stress) coefficients. These residual stress parameters are expressed in dimensionless form by taking: $\alpha_\mathrm{c} = \mu\bar{\alpha}_\mathrm{c}/(2\mathrm{RT})$ and $\alpha_\mathrm{d} = \mu\bar{\alpha}_\mathrm{d}/(2L^5)$, respectively, where $\mathrm{T} = B - A$ is the wall thickness.

The expressions of the stress components in the axial direction have α_d as a coefficient. If $\alpha_d = 0$, then $\sigma_{0\mathrm{ZZ}} = \sigma_{0\mathrm{RZ}} = 0$ and also the other residual stress components reduce to the planar form of the residual stress, with two non-zero components $\sigma_{0\mathrm{RR}}$ and $\sigma_{0\Theta\Theta}$, as it is seen in [17, 19, 44]. In this case, if $\alpha_d = 0$, then α_c can be interpreted as the magnitude of planar residual stresses (see, e.g., [42]. If $\alpha_c = 0$, then the residual stress tensor has the non-zero components $\sigma_{0\mathrm{R}Z}$, $\sigma_{0\Theta\Theta}$, and $\sigma_{0\mathrm{ZZ}}$ when residual stresses occur.

The form of the strain energy W is based on a simple neo-Hookean isotropic energy function with an additional term that accounts for the distribution of the residual stresses in the material [17, 62]:

$$W := \frac{\mu}{2}(I_1 - 3) + \frac{1}{4}(I_6 - \mathrm{tr}\boldsymbol{\sigma}_0), \tag{14}$$

where the different terms are explained in what follows. The first term in (14) is the neo-Hookean (isotropic) model that depends on the shear modulus μ and the first invariant of the right Cauchy-Green deformation tensor $I_1 = \mathrm{tr}\mathbf{C}$. This formulation is commonly used in the modeling of isotropic soft tissue or its constituents. Although it has a relatively simple form, this formulation is supported by experiments since it describes the mechanical behavior of the isotropic component of soft tissue as seen in [63]. Alternative forms of models applicable to isotropic soft tissue behavior include exponential forms or models that combine characteristics of both neo-Hookean and exponential models [49]. The second term of (14) introduces residual stresses and depends on the invariant $I_6 = \mathrm{tr}(\boldsymbol{\sigma}_0\mathbf{C}^2)$ as seen in [17] and [42]. This invariant has units of stress, unlike dimensionless I_1 and other invariants that are necessary to model the anisotropic properties of materials [64]. Higher-order invariants, such as I_6, which is nonlinear, are responsible for a more complex mathematical treatment of residual stresses [17, 19, 20, 41, 60].

In [23], the invariant $I_5 = \mathrm{tr}(\boldsymbol{\sigma}_0\mathbf{C})$ is used, instead of $I_6 = \mathrm{tr}(\boldsymbol{\sigma}_0\mathbf{C}^2)$, to define the second term of the strain energy density of the tube. Here, our purpose is to investigate a neo-Hookean material with an additional term (a second term) associated with the residual stress. This additional term depends on the invariant $I_6 = \mathrm{tr}(\boldsymbol{\sigma}_0\mathbf{C}^2)$, which is a higher-order invariant compared to $I_5 = \mathrm{tr}(\boldsymbol{\sigma}_0\mathbf{C})$. The latter invariant was studied previously, but I_6 did not attract the same attention in the literature. Clearly, the invariant I6 introduces more mathematical complexity than I_5. To fully take account of residual stress, a general approach is necessary, and, in particular, the residual stress needs to feature in the constitutive law for the elastic response of the material, on which we focus in this paper, or for a more general material response. The presence of residual stress introduces specific invariants into the strain energy that penalize deformation. Furthermore, it is important to note that the elastic response of a material with residual stress is non-isotropic. Therefore, the different invariants associated with the residual stress have to be analyzed to quantify and to qualify the material behavior introduced in the model by such stress. . This is not a minor point. Theoretically, the residual stress tensor just satisfies (6) and (7), but to implement the residual stress in the finite element scenario, it is necessary to consider a model. Furthermore, it is important to take into consideration that the elastic response of a model with residual stresses is necessarily anisotropic. It is in this context that the formulation of this paper generalizes the formulation of [23].

It can be seen that when both parameters $\alpha_c = \alpha_d = 0$, the components of the residual stresses tensor $\boldsymbol{\sigma}_0$ are also nullified and the strain energy function (14) reduces to the basic (isotropic) neo-Hookean model.

The problem of the combined extension and inflation of a circular cylindrical tube subject to radial and circumferential residual stresses (i.e $\alpha_d = 0$) and governed by a residual-stress dependent nonlinear elastic constitutive law has been studied in [42]. The corresponding problem for the residual stress at hand (with $\alpha_d \neq 0$ giving an RZ-component of the shear stress) is not ensured to keep its perfect cylinder form under inflation. This motivates our careful finite element analysis, which establishes that a cylindrical form is substantially maintained up to the bifurcation events studied here. This, in turn, motivates the use of certain standard procedures that presume cylindrical symmetry up through the bifurcation events that are the focus of this study. It is also to be remarked that this was also the guiding philosophy in our previous work [23]. Additional commentary on this subject follows in the course of this study.

2.3 Initiation of an instability

The membrane approximation (i.e., no residual stress) applied to a cylindrical shell provides valuable insight into the parameters that play a major role in the triggering of various instability modes. In this section, we delineate these critical thresholds before introducing the detailed numerical framework that follows in this article.

Under combined internal pressure and axial tension, the cylinder maintains its original geometry until at least one of several bifurcation mechanisms is activated. Our primary goal is to determine the conditions under which localized bulging, bending, or prismatic bifurcation develops. This analysis not only clarifies the mechanical factors that initiate the formation of aneurysms [65] but also sheds light on the initiation of closely related vascular disorders [22]. To capture these different bifurcation scenarios, we employ the general incremental-displacement formulation (see Rodriguez & Merodio [3])

$$\delta \mathbf{u} = \delta u_r(\theta, z)\mathbf{e}_r + \delta u_\theta(\theta, z)\mathbf{e}_\theta + \delta u_z(\theta, z)\mathbf{e}_z, \tag{15}$$

where $\{\mathbf{e}_r, \mathbf{e}_\theta, \mathbf{e}_z\}$ are the three base unit vectors of the deformed configuration, and δu_r, δu_θ, δu_z are the components of the incremental displacements.

2.3.1 Bulging for an axisymmetric bifurcation mode

When analyzing bulging for an axisymmetric bifurcation mode, the incremental displacement condition (15) reduces to

$$\delta \mathbf{u} = \delta u_r(z)\ \mathbf{e}_r + \delta u_z(z)\ \mathbf{e}_z, \tag{16}$$

where the azimuthal component of the incremental displacement, δu_θ, is equal to zero, and the remaining two components depend only on the axial coordinate z.

Then, considering the balance of forces in the radial and axial directions of an infinitesimal volume element in the cylinder wall, the actuating forces in equilibrium in the axial direction are

$$\frac{\partial\big[\delta(\sigma_{zz}\, h\, r)\big]}{\partial z}\, \mathrm{d}\theta\, \mathrm{d}z = P\, r\, \mathrm{d}\theta\, \mathrm{d}z\, \frac{\partial \delta u_r}{\partial z}, \tag{17}$$

in which the thickness of the wall is $h = b - a$, r is the radius of the deformed cylinder in the bulging mode, and σ_{zz} is the (Cauchy) axial normal stress. The left side of (17) results from the increase in force in an infinitesimal element of the cylinder wall and is equal to the resulting force due to the pressure in the axial direction.

In the radial direction, the equilibrium follows the expression

$$\delta(\sigma_{\theta\theta}\, h)\, \mathrm{d}\theta\, \mathrm{d}z - \delta(P\, r)\, \mathrm{d}\theta\, \mathrm{d}z = \frac{\partial}{\partial z}\Big[\sigma_{zz}\, h\, r\, \mathrm{d}\theta\, \frac{\partial \delta u_r}{\partial z}\Big]\, \mathrm{d}z, \tag{18}$$

where $\sigma_{\theta\theta}$ is the normal component of the Cauchy stress tensor in the azimuthal direction.

The bifurcation condition under internal pressurization follows directly from the characteristic equation of the coupled system in Eqs. (17) and (18). Rodriguez & Merodio [3] provide a thorough derivation of this result, which is

$$f(\bar{W}, \lambda_\theta, \lambda_z) + \left[\frac{2\pi R}{L}\right]^2 \lambda_\theta^2 \lambda_z \frac{\partial \bar{W}}{\partial \lambda_z} \frac{\partial^2 \bar{W}}{\partial \lambda_z^2} = 0, \tag{19}$$

where

$$f(\bar{W}, \lambda_\theta, \lambda_z) = \lambda_z^2 \frac{\partial^2 \bar{W}}{\partial \lambda_z^2}\left[\lambda_\theta^2 \frac{\partial^2 \bar{W}}{\partial \lambda_\theta^2} - \lambda_\theta \frac{\partial \bar{W}}{\partial \lambda_\theta}\right] \qquad - \left[\lambda_\theta\, \lambda_z \frac{\partial^2 \bar{W}}{\partial \lambda_\theta \partial \lambda_z} - \lambda_\theta \frac{\partial \bar{W}}{\partial \lambda_\theta}\right]^2. \tag{20}$$

It follows that for an infinitely long tube or a long one (L much greater than R), the bifurcation criterion is $f(\bar{W}, \lambda_\theta, \lambda_z) = 0$ in (19). This form (20) has also been shown in various works, such as in Haughton & Ogden [31], Fu et al. [21], Guo et al. [66], and Alhayani et al. [18].

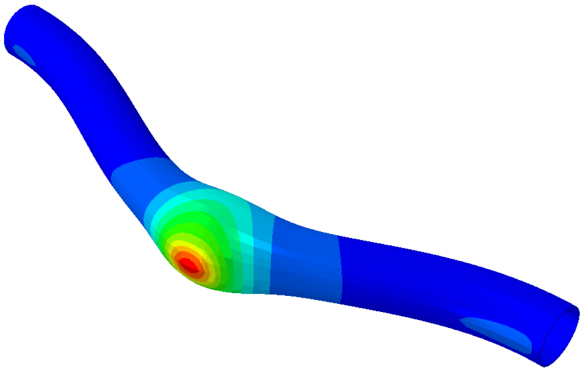

Fig. 1. Post-bifurcation shape of the bending mode for $\lambda_z = 1.02$, $\bar{\alpha}_\text{d} = -15$, and $\bar{\alpha}_\text{c} = 0.5$. A bulge is also shown.

2.3.2 Prismatic Bifurcation

If one allows for non-circular cross-sections, the incremental displacement field simplifies to

$$\delta \boldsymbol{u} = \delta u_r(\theta)\, \boldsymbol{e}_r + \delta u_\theta(\theta)\, \boldsymbol{e}_\theta\,, \tag{21}$$

with an axial increment that is equal to zero ($\delta u_z = 0$) and where both the radial and circumferential components δu_r and δu_θ are functions of the circumferential coordinate θ. In the case of the lowest-energy prismatic mode for a purely membrane response, one finds the simple criterion

$$\frac{\partial^2 \bar{W}}{\partial \lambda_z^2} = 0 \tag{22}$$

as shown in [3].

In the vascular system, tortuosity in the blood vessels often accompanies pathologies such as hypertension, diabetes, or retinal disease [67, 68]. A loss of axial tension can drive vessels to coil or undulate [69], so they deviate from an ideal cylinder. In heavily curved arteries—take the superficial femoral artery, for instance—saccular aneurysms may even develop [70]. Abdominal aortic aneurysms frequently bulge asymmetrically, a phenomenon beyond the reach of uniform-bulge theory. It is therefore essential to examine composite deformations that mix axial twist with local bulging, as in [19].

2.3.3 Bending Bifurcation

The bending bifurcation condition can be expressed as (see [3])

$$\mathcal{M} = \sigma_{\theta\theta} - 2\,\sigma_{zz} = 0\,, \tag{23}$$

where $\mathcal{M} < 0$ indicates stability against bending, and $\mathcal{M} > 0$ signals the onset of a bending instability. In this paper, we are interested in the onset of bifurcation and the subsequent motion, i.e., post-bifurcation, since several modes of bifurcation can occur, one after another. Figure 1 shows on one side of the tube a bulge that is formed during post-bifurcation once the onset of bifurcation occurs.

Although bulging instabilities dominate in many cases, AlChlaihawi et al. [14] and Topol et al. [15] demonstrate that the preferred bifurcation mode depends sensitively on geometry, material properties, loading conditions, and even local changes in tissue microstructure (for example, swelling or inflammation). The membrane-based criteria for bifurcation serve as useful benchmarks for the more detailed numerical studies of thick-walled tubes presented later, where the membrane simplifications are intentionally relaxed. In particular, for instance, the criterion given by $\mathcal{M}$ is used for thick-walled tubes to guide the numerical analysis. There is no analytical solution for the bending bifurcation under these circumstances.

3. Finite Element Analysis

We obtain solutions computationally dealing with a near-perfect cylinder as it is explained in what follows. It is interesting to look for analytical solutions for the (perfect) cylinder at hand, but this is beyond this work. Suffice it to say that the near-perfect cylinder prior to bifurcation behaves as a near-perfect cylinder. Bulging and bending of axially stretched and inflated tubular structures have often been studied in the context of the membrane approximation. These simplified models capture the essential mechanics and frequently serve as a roadmap for more complex scenarios that go beyond the idealized membrane framework, where numerical methods become indispensable ([17]).

The inflation of membrane tubes under axial loading was extensively analyzed using a theory-based approach in earlier work. These investigations required complex mathematical equations; furthermore, they often dealt with basic setups followed by certain simplifications. Numerical methods to explore material models allow the inclusion of more factors that affect the arteries, such as residual stress, plus a number of layers in the wall.

To mimic the behavior of an artery, researchers build material models and study them with the commercial software `Abaqus`. This section covers the main features, such as shape, chosen element type, and boundary conditions. Yet, it is important to capture the effect of each factor, apart from the material itself.

3.1 Finite element model

A finite element model is developed in `Abaqus` in order to study the tubes subjected to axial pre-stretches and loaded with internal pressure, incorporating three-dimensional residual stress in an initial step. A complete cylindrical tube is created, as axisymmetric simplification cannot be used due to restrictions on the constitutive equations of the material.

We have developed a finite element model that shows the quantitative and qualitative capability of this methodology to capture bifurcation and post-critical behavior. The (general) description of the finite element model is as follows (see [37] for further details and [71]).

1. A tube (geometry) is created. To avoid a strict numerical bifurcation, a small imperfection is introduced. One imperfection to capture bulging, for instance (there are others), is to create a deviation along the axis of the tube, a maximum deviation of $10^{-4}R$ (for instance) increasing from one end of the tube to the other end of the tube. Bending bifurcation is established by following the initiation of lateral movement of the tube. Subsequently, post-bifurcation analysis is done, introducing a geometric imperfection. This is necessary to obtain a smooth solution path. The scale of imperfection is applied based on the first eigenmode, and the factor is a maximum magnitude of $5{\times}10^{-3}$ times the radius.

2. The material. It is necessary to define the strain energy as a function of the prestress. It has not been implemented yet in any finite element commercial code. The material model has been implemented in Abaqus as a subroutine (UMAT) to be used for incompressible hybrid elements. The user must provide the Cauchy stress tensor. In particular, the deviatoric stress must be provided for a fully incompressible user material.

3. The mesh. It is important to deal with the so-called "hourglass". Abaqus has special features for this. The enhanced hourglass control approach represents a refinement of the pure stiffness method in which the stiffness coefficients are based on the enhanced assumed strain method; no scale factor is required. It provides more suitable resistance to hourglassing for nonlinear materials. The artificial energy is provided to be compared with the overall internal energy. When it is not deemed negligible, it is recommended to use a finer mesh. In practice, if we see an "hourglass" control energy greater than 1% or 2%, we run the analysis with more elements in the thickness in the flexural areas and verify that the results of interest are not significantly affected.

4. The nonlinear finite element analysis is run (see Fig. 4). It is worth clarifying that with this strategy, we do not determine exactly the bifurcation point. This point corresponds with the state for which the tangent stiffness matrix becomes singular. In fact, we avoid the precise bifurcation point by introducing the imperfection. When the solution violates a symmetry (in our case, based on the history of two control points), one estimates the associated state as critical.

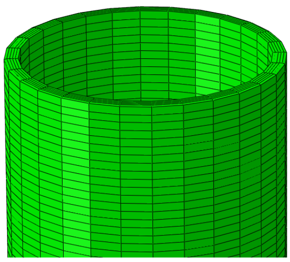

Fig. 2. Finite element mesh of the cylinder model in `Abaqus`.

The elements used for the mesh are the `C3D8RH` 8-node linear brick elements, which are available in the library of `Abaqus`. The built-in hybrid formulation, as seen in the documentation [45], is used for an incompressible material to mitigate the strain-locking problem. Figure 2 provides a typical mesh of a cylindrical tube.

Meshes of different sizes were tried for the model using several settings, such as the level of stretch along the axis, and tests were run to check this influence. To show the various instability effects clearly, in general, 64 elements were placed in the azimuthal direction, plus five elements through the wall thickness. In the length direction, 200 to 350 elements were used. Nevertheless, in the models used to capture bulging bifurcation, sometimes more than 64 elements were used in the azimuthal direction, depending on the axial stretch.

An imperfection is applied to the model to capture bifurcation. Clearly, the mechanical behavior of the inflated and stretched cylinder may change with small imperfections, so a sensitivity analysis is necessary to rule out that the imperfection affects the results (see [72]). `Abaqus` can implement a modified Riks method with an analysis that involves a finite number of steps in order to find the *equilibrium path* which follows the solution. The added small imperfection is used accordingly to obtain two bifurcation modes in this work, the bulging and bending ones.

The general dimensions of the cylindrical tube are: a mean diameter of D $= 10$ mm, a wall thickness of T $= 0.50$ mm, and a length of L $= 150$ mm, for which L/D $= 15$ and T/D $= 0.05$.

The distribution of residual stresses along the thickness is shown in Fig. 3. The variation in setting different values of $\bar{\alpha}_{\rm d}$ and $\bar{\alpha}_{\rm c}$ is also observed: Figs. 3 (a) to (c) make use of $\bar{\alpha}_{\rm d} = 15$ and $\bar{\alpha}_{\rm c} = 0.5$; Figs. 3 (d) to (f) make use of $\bar{\alpha}_{\rm d} = -15$ and $\bar{\alpha}_{\rm c} = 0.5$; Figs. 3 (g) make use of $\bar{\alpha}_{\rm d} = -15$ and $\bar{\alpha}_{\rm c} = -0.5$. The stress components are normalized with respect to the material constant μ.

3.2 Analysis procedure

The mechanical constitutive behavior is represented by a formulation code, introduced via an `Abaqus` user subroutine (`UMAT`), which can be used with incompressible elastic materials via SDVINI. The nonlinear analysis is composed of three distinct incrementally applied steps (see Fig. 4).

In the initial step, the residual stress field described in (13) is integrated into the cylindrical tube. First, one must select the residual-stress parameters. A sensitivity analysis with an incremental magnitude of the residual stresses is performed for a couple of reasons: to evaluate the resulting stresses and the associated equilibrium of the model (the finite element program obtains the equilibrium of the cylinder), and also to find a stable configuration for the following bifurcation analysis. The following values of the parameters are chosen based on the results of that analysis: $\bar{\alpha}_{\rm d} \in \{-15, 0, 15\}$ and $\bar{\alpha}_{\rm c} \in \{-0.5, 0, 0.5\}$. Some results are presented in Figs. 5 - 6 for the selected values $\bar{\alpha}_{\rm d} = -15$ and $\bar{\alpha}_{\rm c} = 0.5$: Figure 5 presents the distribution of von Mises stresses in a contour graph of the cross-sectional area near the mid-span of the tube. The stresses are relatively larger in magnitude on the outer and inner walls, while they are smaller in the center of the wall. Figure 6 shows the distribution of the axial normal stresses (σ_{0zz}) for the same location. Moving from the inner wall to the outer wall, these axial stresses increase from negative values (compressive stresses) to positive values (tensile stresses). If the results from Figs. 5 - 6 are compared to similar Figs. 4-5 in article [23], then it can be shown that the variation of the residual stresses and the extreme value are larger in this paper, when the strain energy density function (14) includes the invariant I_6 as opposed to the use of the invariant I_5 in [23].

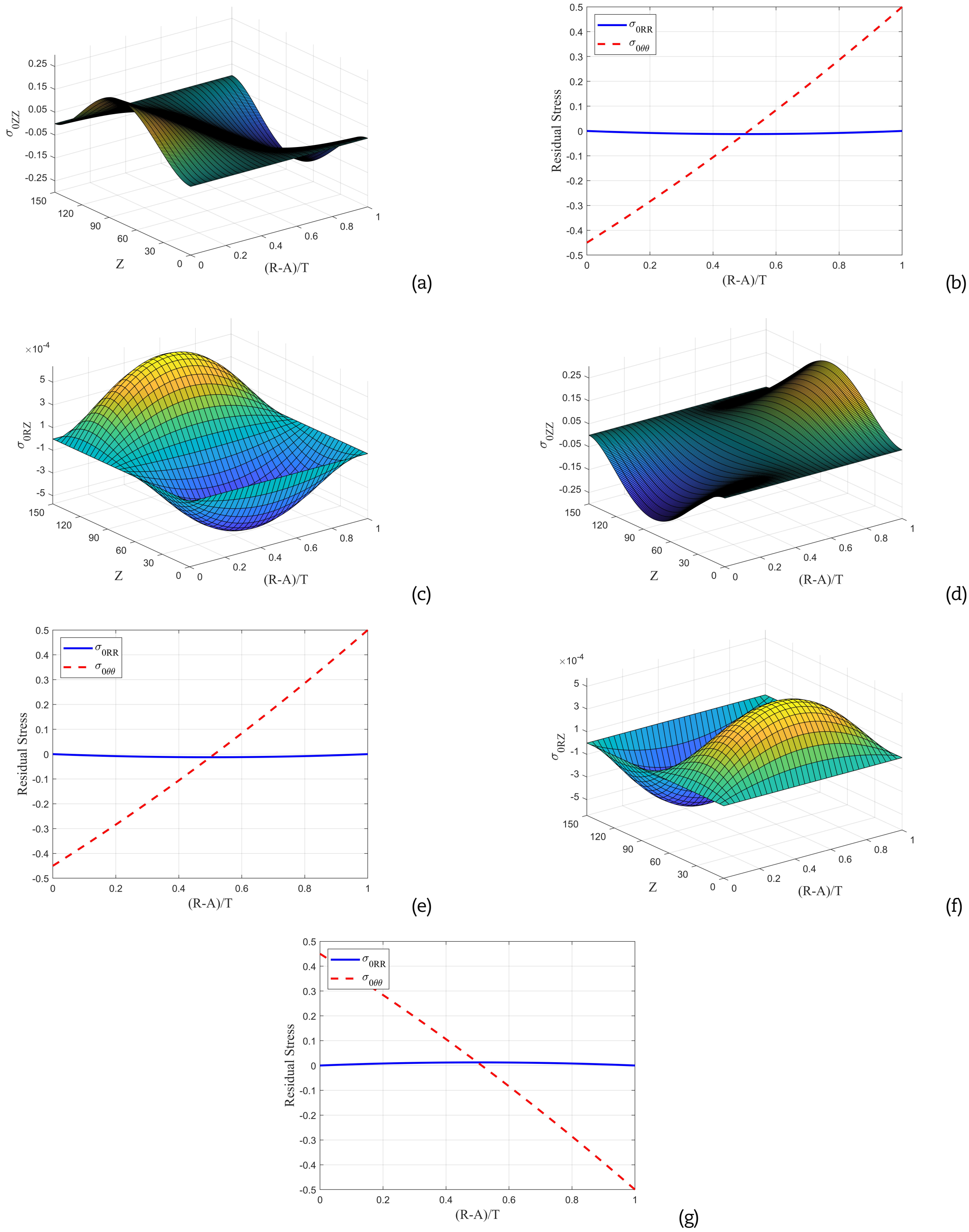

Fig. 3. Distribution of residual stresses at the end of the first step. The panels (a) to (c) make use of $\bar{\alpha}_d = 15$ and $\bar{\alpha}_c = 0.5$; the panels (d) to (f) make us of $\bar{\alpha}_d = -15$ and $\bar{\alpha}_c = 0.5$; the panel (g) makes use of $\bar{\alpha}_d = -15$ and $\bar{\alpha}_c = -0.5$. Note that the effect of the second term on the right side of $\sigma_{0\Theta\Theta}$ (see Eqs. (10) and (13)) is negligible compared with the other term; therefore, only the planar term is shown.

In the second step, axial pre-stretches are imposed at one end of the tube, while the other end is fixed in the axial direction. The axial stretch is also applied incrementally, starting from the configuration of the previous and first step, and it stops once the final length is reached.

Finally, uniform internal pressure $p = 10\mu T/D$ is applied in the third step. The mechanical response is represented by the load proportionality factor plot against the arc length, as seen in Figure 7, which provides a typical curve of the load proportionality factor (LPF) versus the arc length relationship [45]. The applied internal pressure is expected to increase with an increasing arc length, and consequently, the peak point will be easily captured. Therefore, both bifurcation and post-bifurcation patterns can be captured.

A combination of simulations is necessary to capture bifurcation and postbifurcation. Hoop displacements are restricted in a simulation to obtain just the bulging bifurcation. However, that movement is permitted to obtain the bending mode. To identify the onset of the bulging mode, it is appropriate to compare the displacements of two points along the cylinder's length: one outside the bulge and the other within the bulge. When analyzing the pressure versus azimuthal stretch curve for these two points, the two

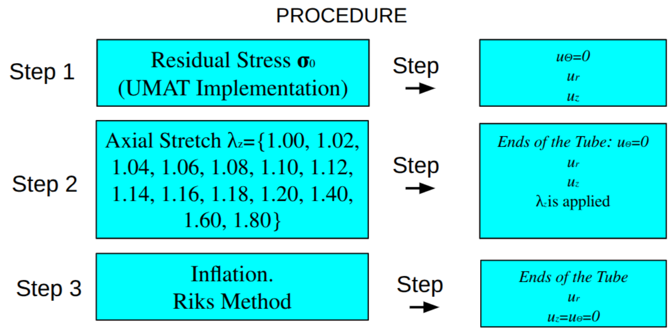

Fig. 4. The nonlinear analysis is composed of three distinct incrementally applied steps.

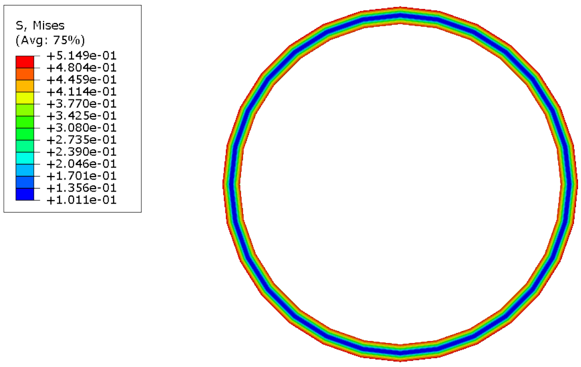

Fig. 5. Distribution of the von Mises stresses in a contour plot of the cross-sectional area near the mid-span of the tube. The stresses are relatively large at the outer and inner walls, with the minimum in between.

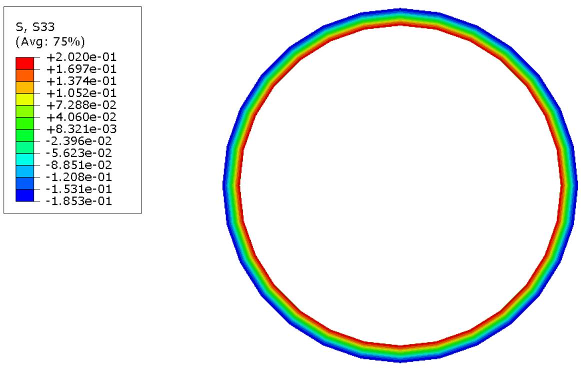

Fig. 6. Distribution of the axial normal residual stresses (σ_{0zz}) for the same location as in Fig. 5. Going from the outer to the inner wall, these axial stresses increase from negative values (compressive stresses) to positive values (tensile stresses).

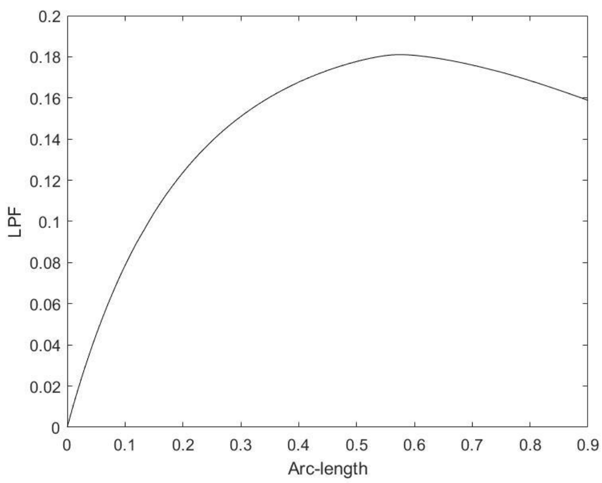

Fig. 7. An instability is expected when the load proportionality factor (LPF) reaches its maximum value in this plot in terms of the arc length.

Table 1. Combinations of the parameters $\bar{\alpha}_c$ and $\bar{\alpha}_d$ that define the magnitude and distributions of the residual stresses. Case 7 nullifies the residual stress tensor, and the material model behaves as the basic neo-Hookean material.

Case	$\bar{\alpha}_d$	$\bar{\alpha}_c$
Case 1	15	0.5
Case 2	15	-0.5
Case 3	-15	0.5
Case 4	-15	-0.5
Case 5	15	0
Case 6	-15	0
Case 7	0	0
Case 8	0	0.5
Case 9	0	-0.5

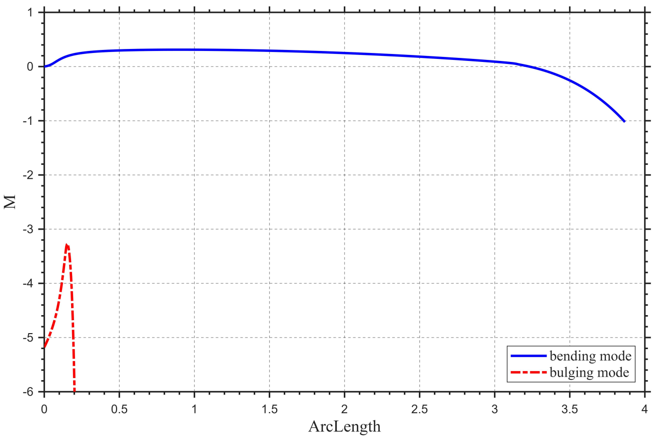

Fig. 8. The profile of $\mathcal{M} = \sigma_{\theta\theta} - 2\sigma_{zz}$ versus arc length are presented for two (bifurcated) models, Case 1 with $\lambda_z = 1$ (solid line) and Case 1 with $\lambda_z = 1.4$ (dashed line), at a cross-section, for each model, associated with maximum stress values. In Case 1 with $\lambda_z = 1$, the curve shows that $\mathcal{M} = \sigma_{\theta\theta} - 2\sigma_{zz} > 0$, suggesting that bending is the bifurcation mode. In contrast, for Case 1 with $\lambda_z = 1.4$, the curve shows values $\mathcal{M} = \sigma_{\theta\theta} - 2\sigma_{zz} < 0$, implying that bending is unlikely to be the bifurcation mode, and that bulging is the bifurcation mode instead.

curves depart as the hoop stretch changes between these two points of the cylinder, i.e., the departure point of these two curves is the onset of (bulging) bifurcation. This mechanism will be illustrated in Section 4..

The bending criterion of the membrane analysis $\mathcal{M} = \sigma_{\theta\theta} - 2\sigma_{zz} > 0$ will be considered to capture the bending instability during the inflation step. The numerical calculations from [22] propose that there are different asymmetric bifurcation modes; however, the first and most likely mode under quasi-static conditions is the one that fits the criteria in this work. The bending bifurcation mode is illustrated in Fig. 1.

The critical pressure is determined using the modified Riks analysis procedure (ABAQUS terminology for the arc-length method). It is a very efficient method for solving non-linear systems of equations when the problem under consideration may exhibit snapping behavior. In this procedure, the concept of time is replaced by arc length. This method postulates a simultaneous variation in both the displacements and the load proportional factor (LPF) and is an indicator of the applied load and the evolution of deformation, respectively (see Fig. 7 and Fig. 9). It is a two-step simulation process. Further details are presented in [37].

4. Numerical Results

Nine (different) combinations of the parameters $\bar{\alpha}_d$ and $\bar{\alpha}_c$ are selected based on the (sensitivity) analysis mentioned in Section 3.2. These combinations are labeled as "Case 1", "Case 2", ..., "Case 9", and presented in Table 1. This section aims to illustrate and discuss the combined effect of varying axial stretches, when axial stretch is in the range $1 < \lambda_z < 1.8$, and applied internal pressure, along with non-planar residual stresses, on the response of the numerical models. The numerical results contrasting the nine cases are presented.

Section 2.3 explains the conditions associated with the onset of bulging (axisymmetric) as well as the onset of bending (asymmetric). The numerical results capture these conditions and the differences in the deformed tubes when the onset of bifurcation occurs either through bulging or bending.

4.1 Approach to capture the two modes of instability

To understand the interplay between the stress distribution and the effect that the combinations of the parameters $\bar{\alpha}_c$ and $\bar{\alpha}_d$ have on the onset of the considered bifurcation modes, it is crucial to clarify a methodological distinction between the two modes - bending and bulging - examined in this study.

The bending criteria (23) from the membrane analysis will be examined through the numerical analyses; the relationship between $\mathcal{M}$ and the arc length throughout the deformation analysis is plotted. If during the analysis the curve obtained at a particular cross-section has positive values (that is, $\mathcal{M} > 0$), it can be validated that the obtained mode is bending. In contrast, if the curve is negative (that is, $\mathcal{M} < 0$), the bending mode is not expected. In Figure 8 it can be seen how the bending criteria ($\mathcal{M}$) behaves differently for two cylinders in which bifurcation occurs: one cylinder is Case 1 material model with $\lambda_z = 1$, associated with bending bifurcation, develops the solid line, while Case 1 with $\lambda_z = 1.4$, the second cylinder, associated with bulging bifurcation, develops the dashed line (in this case $\mathcal{M} < 0$, bending is not expected).

We now take a different approach to further illustrate these results, considering two models for just Case 1 with $\lambda_z = 1$. In one

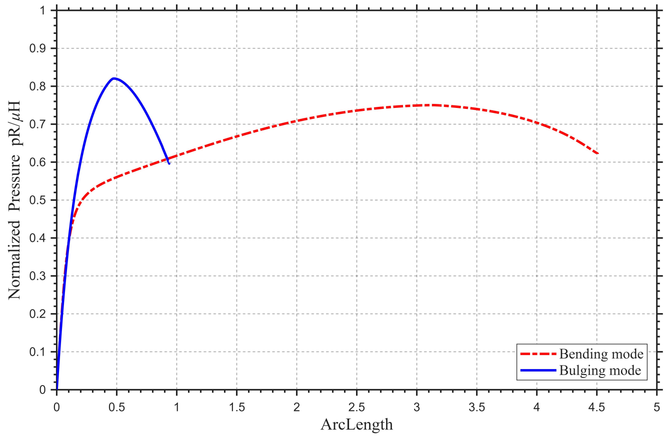

Fig. 9. Normalized pressure vs. arc length for Case 1 with $\lambda_z = 1$ is depicted. The solid line represents the model constrained to capture only the bulging mode, whereas the dashed line corresponds to the general model, which is unrestricted. The point at which the two curves diverge is identified as the bending bifurcation point. The maximum points of the two curves, beyond which the structure cannot withstand additional load, are the bulging bifurcation points. The maximum point of the dashed line is associated with the formation of a one-sided bulge. On the other hand, the other maximum point is associated with the formation of an axisymmetric bulge.

of the models to capture of just bulging hoop displacements is prevented. In Fig. 9, the normalized pressure values for this model are plotted in terms of the arc length values as a solid line. This is a curve associated with (axisymmetric) bulging, which appears at the maximum point. In the other model, hoop displacements are not restricted. In Fig. 9, the normalized pressure values for that particular model are also plotted in terms of the arc length values as a dashed line. For this latter model, bending occurs when the two curves in the Figure depart, and later on, a bulge appears at the maximum point of the (dashed) curve (see Figure 1 for a representation of the deformed tube). In both curves, the maximum is associated with a bulging bifurcation; afterward, the internal pressure decreases.

According to the results from Figs. 8 and Fig. 9, it is possible to obtain the bulging bifurcation mode for the entire range of axial stretches $1 < \lambda_z < 1.8$ that is used in the different examples of this article. However, the bending mode is expected for small values of the axial stretch range; the bending mode becomes likely as the axial stretch approaches $\lambda_z = 1$. To clarify these aspects, we will focus on different analyses with different models. First, we will focus on bulging.

4.2 Bulging analysis

We deal with many models and try to establish their behavior with regard to the onset and propagation of bifurcation. Nevertheless, we expect to get bulging for sufficiently large values of the axial stretch. With this in mind, we analyze first that scenario and later on, small values of the axial stretch.

4.2.1 Comparison of stress distribution: Case 1 and Case 3 from Table (1), taking $\lambda_z = 1.6$

We expect to get bulging and, indeed, that is the case. A bulge may appear at different axial locations of the tube, depending on the distribution of the residual stresses. This is illustrated in Fig. 10, where cases 1 and 3 from Table 1 are compared. For Case 3 the parameter $\bar{\alpha}_{\mathrm{d}}$ is negative and the bulge appears in the middle section (see Fig. 10(c)); however, when the parameter $\bar{\alpha}_{\mathrm{d}}$ is positive in Case 3, the bulge appears at one of the ends of the tube (see Fig. 10(d)).

Both figures 10(a) and 10(b) include graphs of the average axial and azimuthal stresses $\sigma_{\theta\theta}$ and σ_{zz} along the axial direction of the tube; the maximum values match the positions of the bulge mentioned above. In Fig. 10 (a), both axial stresses and hoop stresses increase until they approach their maximum magnitude near the center, following a decrease towards the end. In Fig. 10 (b), both axial stresses and hoop stresses decrease until they approach a minimum near the center, after which they again increase to reach the maximum magnitude at the end of the tube.

Although the sign of $\bar{\alpha}_{\mathrm{d}}$ influences the position of the bulge obtained in an analysis, $\bar{\alpha}_{\mathrm{c}}$ does not affect the qualitative nature of the bulge.

4.2.2 Normalized inflation pressure versus axial stretch at the maximum inflation point

We broaden our analysis now to consider all possible values of axial stretch. We focus on bulging and restrict hoop displacements to capture only that bifurcation. The maximum load-bearing capacity during an analysis occurs at the onset of a bulging bifurcation. This value is studied in terms of the axial stretch applied in Step 2 (see Section 3.2) as seen in Figure 11. This value gradually decreases as λ_z takes higher values; this applies to all cases in Table 1, and the phenomenon is seen in [49].

In order to visualize and compare how the residual stresses modify this behavior, the normalized inflation pressure is plotted for models for all nine residual stress distribution cases. It is also noticeable how $\bar{\alpha}_{\mathrm{d}}$ and $\bar{\alpha}_{\mathrm{c}}$ modify the overall load capacity of the tubes and influence the formation, development, and location of the bulge along the tube; is clear when comparing Case 7 against cases with positive values of $\bar{\alpha}_{\mathrm{d}}$. The parameter $\bar{\alpha}_{\mathrm{d}}$ is relevant when considering cases that share an equal value for $\bar{\alpha}_{\mathrm{c}}$, as positive values reduce the normalized pressure proportionally.

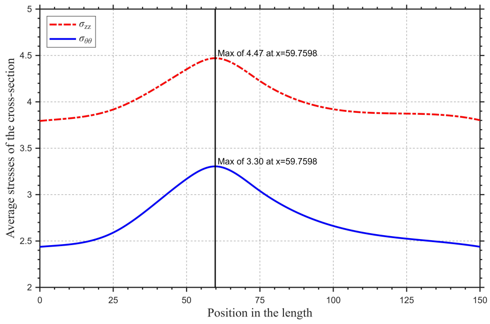

(a) Values of azimuthal and axial average stresses on each cross-section along the tube length, taking $\bar{\alpha}_\mathrm{d} = -15$ and $\bar{\alpha}_\mathrm{c} = 0.5$, $\lambda_z = 1.6$.

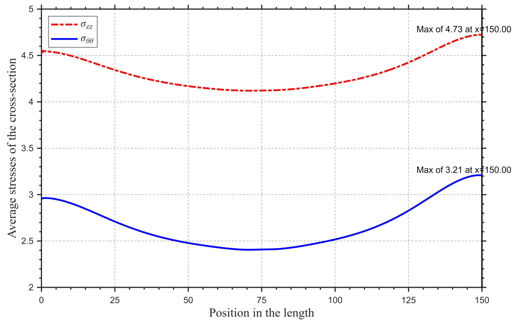

(b) Values of azimuthal and axial average stresses on each cross-section along the tube length, taking $\bar{\alpha}_\mathrm{d} = 15$ and $\bar{\alpha}_\mathrm{c} = 0.5$, $\lambda_z = 1.6$.

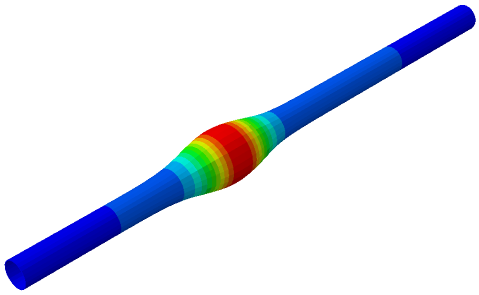

(c) Post-bifurcation of bending instability bulging instability in the middle of the cylinder associated with Fig. 10 (a)

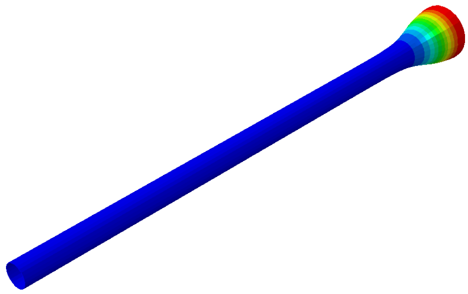

(d) Post-bifurcation of bending instability bulging instability at both ends of the cylinder associated with Fig. 10 (b)

Fig. 10. Differences in the location of the bulge for the cylinders for the cases 1 and 3 for the residual stress parameters $\bar{\alpha}_\mathrm{d}$ and $\bar{\alpha}_\mathrm{c}$ (see Table 1).

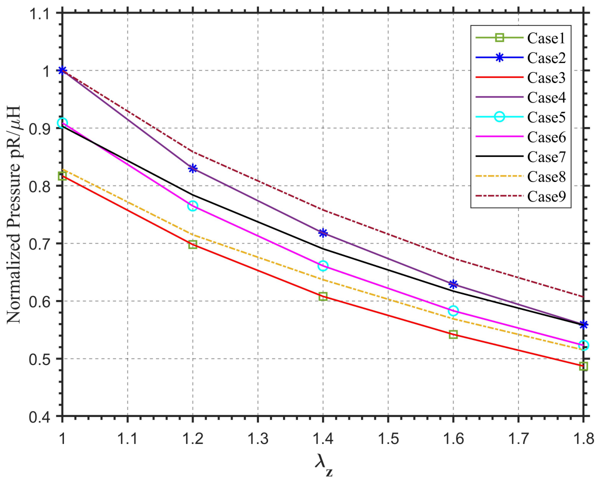

Fig. 11. Normalized inflation pressure in terms of axial stretches at the bulging bifurcation point for cases from Table 1. Hoop displacements are restricted to capture just bulging.

Figure 11 shows a similar behavior (overlapping curves in the figure) between case 1 and case 3 for which $\bar{\alpha}_c$ is equal to 0.5, and similarly between case 5 and case 6, with $\bar{\alpha}_c$ equal to zero, and between case 2 and case 4 with $\bar{\alpha}_c$ equal to -0.5.

4.2.3 Normalized inflation pressure versus azimuthal stretch during inflation, including formation and propagation of bulging

The hoop stretch $\lambda_\theta = r/R$ that accounts for the average nodal displacements of the wall in the cross-sectional plane is an appropriate measure of the bulging phenomenon. Figure 12 illustrates how this stretch varies during a bulging mode analysis in two different sections of the cylinder tube, one point is located in the bulge (IN), and the other point is located outside the bulge (OUT).

The stretch profiles of these two points remain qualitatively similar, suggesting that radial displacements are fairly uniform until the normalized pressure approaches its peak near the bifurcation point, after which the bulge begins to propagate. For the section located inside the bulge, the curves reveal a reduction in the pressure as the circumferential stretch increases, indicating that inflation continues even as the sustained pressure drops. At the second observation point, the response matches that of the first point up to the maximum pressure. Beyond this stage, however, both the pressure and the circumferential stretch diminish, reflecting a deflation process. Figure 12, obtained for Case 3 ($\bar{\alpha}_\mathrm{d} = -15$, $\bar{\alpha}_\mathrm{c} = 0.5$), presents results for pre-stretch values $\lambda_z = 1.0, 1.2, 1.4, 1.6$, and 1.8. In this figure, the dashed curve corresponds to the first location inside the bulge, while the solid curve traces the behavior of the second point over the entire pressure loading history.

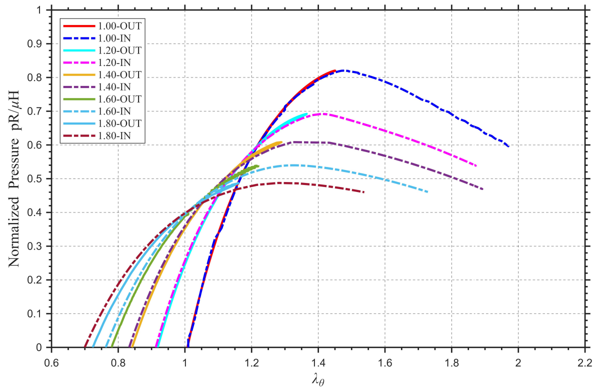

Fig. 12. Normalized inflation pressure in terms of hoop stretch λ_θ, taking $\bar{\alpha}_\text{d} = -15$ and $\bar{\alpha}_\text{c} = 0.5$, for two locations on the tube: one point is located inside the bulge (IN) and the other point is located outside the bulge (OUT). The different curves are for different axial stretches: $\lambda_z = 1.0$ (”100-OUT”, ”100-IN”), $\lambda_z = 1.2$ (”120-OUT”, ”120-IN”), $\lambda_z = 1.4$ (”140-OUT”, ”140-IN”), $\lambda_z = 1.6$ (”160-OUT”, ”160-IN”), $\lambda_z = 1.0$ (”180-OUT”, ”180-IN”).
.

4.2.4 Influence of Axial Stretching on Stress Distributions

This section aims to describe the relationship between axial stretch and the resulting stress distributions in both the axial and azimuthal directions. Figure 13 presents the variation of the average axial stress, σ_{zz}, and azimuthal stress, $\sigma_{\theta\theta}$, along the tube for two values of the axial stretches, $\lambda_z = 1.2$ and $\lambda_z = 1.6$, at the onset of bifurcation.

In Fig. 13(a), corresponding to $\bar{\alpha}$d $= -15$ and $\bar{\alpha}$c $= 0.5$ (Case 3), the average axial stress along the tube's length increases with higher axial stretch λ_z. In contrast, the azimuthal stress at bifurcation is greater for $\lambda_z = 1.2$ than for $\lambda_z = 1.6$.

A similar trend is observed when comparing Case 3 with Case 1: in both cases, the average axial stress is higher at larger λ_z, while the azimuthal stress is higher at $\lambda_z = 1.2$ than at $\lambda_z = 1.6$. However, the locations of the peak stresses differ, occurring near the mid-section of the tube in Case 3 and closer to the ends in Case 1. Nevertheless, the profiles shown by these plots are associated with bulging, i.e., there are maximum values of axial and azimuthal stresses at the cross sections in which bulging appears.

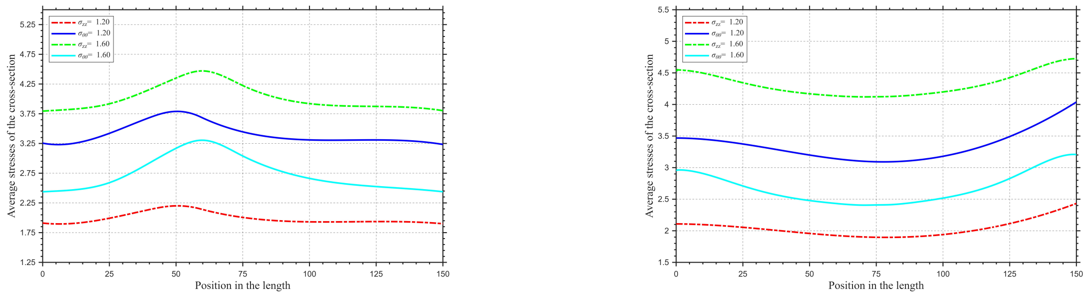

(a) Values of azimuthal and axial average stresses on each cross-section along the tube length for $\bar{\alpha}_\text{d} = -15$ and $\bar{\alpha}_\text{c} = 0.5$, (Case 3), taking two values for the axial stretches, $\lambda_z = 1.2$ and $\lambda_z = 1.6$.

(b) Values of azimuthal and axial average stresses on each cross-section along the tube length for $\bar{\alpha}_\text{d} = 15$ and $\bar{\alpha}_\text{c} = 0.5$, (Case 1), taking two values for the axial stretches, $\lambda_z = 1.2$ and $\lambda_z = 1.6$.

Fig. 13. Effect of increasing the axial stretches on the distributions of stress components for a bulging instability.

4.3 Bending bifurcation and bulging bifurcation

The previous section examined bulging restricting hoop displacements in some of the models, in particular, in the ones with small values of the axial stretch. Now, this restriction no longer holds in any model. The goal is to establish the bifurcation behaviour of the models with respect to axial stretch. For small values of axial stretch, we expect to get bending, and we dedicate our effort first to that scenario with small values of the axial stretch.

4.3.1 Stress distribution for Case 1 and Case 3, taking $\lambda_z = 1.10$

Bending gives the onset of bifurcation, and here the numerical results for these models (undergoing bending bifurcation) are presented following a parallel procedure to the analysis of bulging bifurcation in Section 4.2.1. Figures 14 and 15 illustrate the average values for the axial stress σ_{zz} and for the hoop stress $\sigma_{\theta\theta}$ along the cylinder length for Case 3 and Case 1 (see Table 1), taking an axial stretch of $\lambda_z = 1.10$.

Figure 14 (a) shows the average axial and azimuthal stresses at each cross section for $\bar{\alpha}_\text{d} = -15$ and $\bar{\alpha}_\text{c} = 0.5$ (Case 3) at the onset of bending instability. In a similar fashion, Fig. 15(a) presents the corresponding stress distributions for $\bar{\alpha}_\text{d} = -15$ and $\bar{\alpha}_\text{c} = 0.5$ (Case 1). In both cases, the curves reveal a nearly uniform stress profile along the tube length at the bifurcation point.

Post-bifurcation behavior is illustrated in Figures 14(b) and 15(b). For Case 3, Figure 14(b) shows that both the axial stresses σ_{zz} and the hoop stresses $\sigma_{\theta\theta}$ reach their maximum values near the midsection of the tube. The corresponding tube shapes are depicted in Figs. 14 (c) and (d), representing the onset of bending and the post-bifurcation stage, respectively. At this later stage, a lateral bulge develops precisely where the stresses peak.

For Case 1, Fig. 15 (b) indicates that the maximum stress values occur near one end of the tube, while the lowest values are located in the middle. Figures 15 (c) and (d) display the tube configurations at the onset of bending and in the post-bifurcation stage, respectively, where a bulge is observed forming at the tube's end.

Overall, the stress distributions in Figs. 14 (a) and 15 (a) suggest that before the onset of bending bifurcation takes place, the mechanical response for both Case 1 and Case 3 is qualitatively almost identical. The difference emerges after bifurcation, where the residual stress parameters lead to distinct post-bifurcation patterns, both in the location of maximum stresses and in the position of the bulges along the tube.

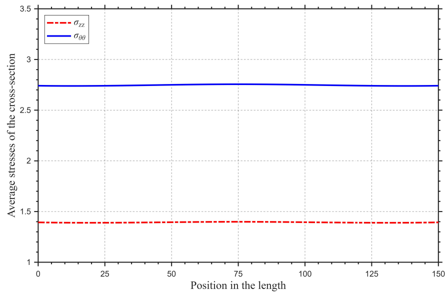

(a) Values of azimuthal and axial average stresses on each cross-section along the tube length for $\bar{\alpha}_{\rm d} = -15$ and $\bar{\alpha}_{\rm c} = 0.5$, $\lambda_z = 1.10$ at the bending instability.

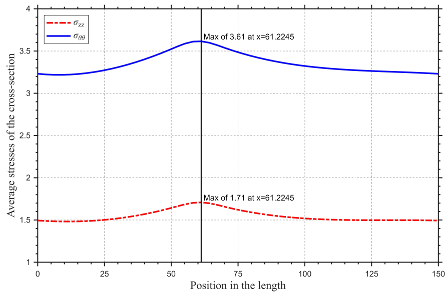

(b) Values of azimuthal and axial average stresses on each cross-section along the tube length for $\bar{\alpha}_{\rm d} = -15$ and $\bar{\alpha}_{\rm c} = 0.5$, $\lambda_z = 1.10$ at the bulging instability after bending bifurcation.

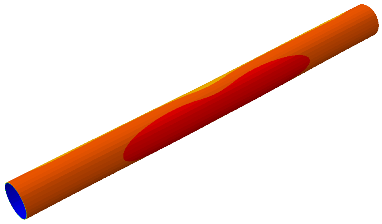

(c) Bending instability of the cylinder associated with Figure 14 (a).

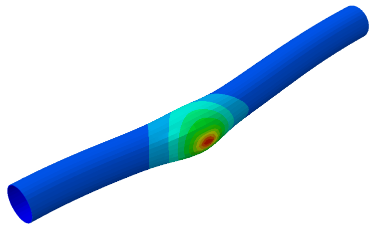

(d) Post-bifurcation of bending instability at a section close to the middle cross-section of the cylinder associated with Figure 14 (b)

Fig. 14. Different bulge locations of the cases with different residual stress parameters

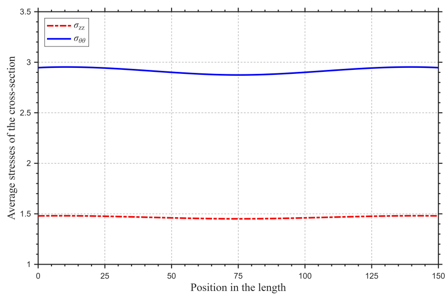

(a) Values of azimuthal and axial average stresses on each cross-section along the tube length for $\bar{\alpha}_{\rm d} = 15$ and $\bar{\alpha}_{\rm c} = 0.5$, $\lambda_z = 1.10$ at the bending instability

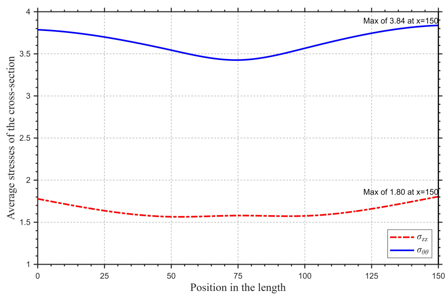

(b) Values of azimuthal and axial average stresses on each cross-section along the tube length for $\bar{\alpha}_{\rm d} = 15$ and $\bar{\alpha}_{\rm c} = 0.5$, $\lambda_z = 1.10$ at the bulging instability after bending bifurcation

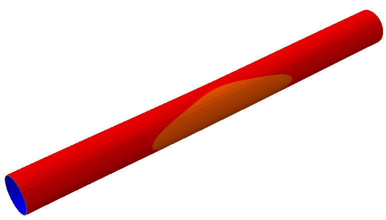

(c) Bending instability in the cylinder associated with Figure 15 (a)

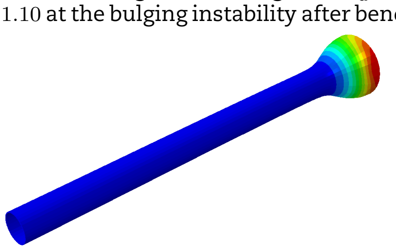

(d) Post-bifurcation of bending instability at the ends cross-section of the cylinder associated with Figure 15 (b)

Fig. 15. Different bulge locations of the cases with different residual stress parameters

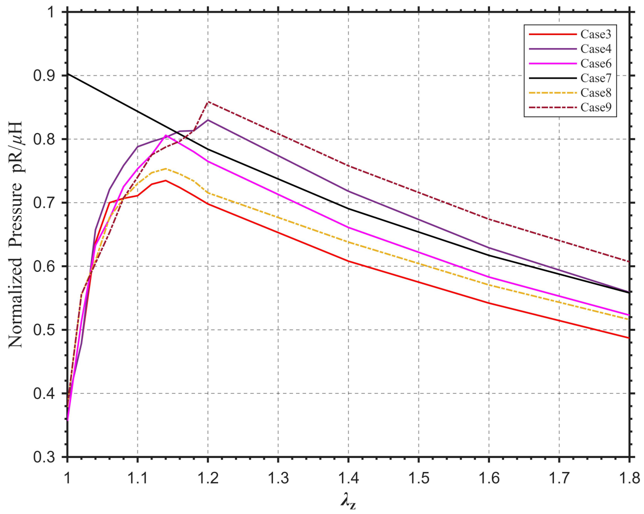

Fig. 16. Normalized inflation pressure versus axial stretches at the bifurcation point for selected residual stress distributions.

4.3.2 Normalized inflation pressure versus axial stretch at the onset of bifurcation

The normalized pressure at each (first) bifurcation point is plotted in Fig. 16 as a function of the axial stretch λ_z for Cases 3–9. A simple comparison of Fig. 16 and Figure 11 establishes the following. The bending bifurcation curve is present over an initial range of λ_z, showing an upward trend, i.e., for small values of the axial stretch, the onset of bifurcation is found to be the bending mode. This curve (for each model) rises only up to a certain threshold; beyond this limiting value, the instability switches from bending to bulging. The transition occurs when the pressure-inducing bending matches the pressure that triggers one-sided bulging. Although the precise limits differ among the cases in Table 1, the transition range generally falls within $1.14 < \lambda_z < 1.2$.

The change in instability mode is illustrated more clearly in Fig. 17 for Case 3. Once the bending bifurcation curve surpasses the bulging curve at $\lambda_z > 1.14$, bulging becomes the dominant mode at onset. For a given axial stretch, after the bending mode initiates (dash-dotted line), the model can sustain further pressure until a critical point, at which localized one-sided bulging appears (dotted line). The resulting irregular deformation is reminiscent of that observed in abdominal aortic aneurysms (AAA), as previously discussed.

Figure 17 presents the normalized pressure values for bulging instabilities triggered after bending has occurred. The pressure associated with pure bulging onset (hoop displacements are restricted) is consistently higher. This suggests that delaying the onset of bending may also delay the formation of aneurysms. For larger values of the axial stretch λ_z, the pressures for the two modes approach each other, as shown beyond the limit point ($\lambda_z = 1.14$) in Fig. 17.

4.3.3 Role of increasing axial stretch in post-bifurcation behavior

This section examines further the post-bifurcation configurations that develop once instability begins. Figure 18 compares the instability patterns for all nine residual stress distributions listed in Table 1, using an applied axial stretch of $\lambda_z = 1.6$. In cases where $\bar{\alpha}_\mathrm{d} = 0$ and the residual stress tensor is limited to planar components, the bulge consistently forms at the midpoint of the tube, highlighting the role of axial residual stresses in controlling bulge location.

Post-bifurcation shapes for the bending mode are shown in Fig. 19. These correspond to Case 3, with $\bar{\alpha}_\mathrm{d} = -15$ and $\bar{\alpha}_\mathrm{c} = 0.5$, for axial stretch ratios increasing from $\lambda_z = 1.00$ in panel (a) to $\lambda_z = 1.20$ in panel (k), in increments of $\Delta\lambda_z = 0.02$. At lower axial stretches, the bulge forms laterally and has an irregular outline—again resembling AAA morphology [36]. As the axial stretch increases, the instability evolves toward a more symmetric, pure bulging configuration, as seen in panels (l) to (n) of Fig. 19.

4.3.4 Development of the post-bifurcation configuration

The different panels of Fig. 20 illustrate how a bulging instability develops, beginning at its onset and progressing step by step to the fully formed post-bifurcation state. The model examined here utilizes the residual stress parameters from Case 3, with the analysis performed at an axial stretch of $\lambda_z = 1.40$. In this case, the instability initiates as a bulging mode.

Similarly, Fig. 21 presents the sequence of configurations showing the formation and propagation of a one-sided bulge for the same Case 3 material. As described in Section 3., lateral motion was restricted to capture the bulging behavior shown in Figure 20, whereas in the cylindrical model, lateral bending was permitted to capture the bending mode seen in Figure 21.

Finally, Figure 22 shows the configuration history for a cylindrical tube, again with the Case 3 residual stress parameters, but with an axial stretch of $\lambda_z = 1.14$, representing a limit or transitional value. Here, it is evident that axial stretch influences the post-bifurcation shape: the bulge evolves from the one-sided form seen in Figure 21 toward the nearly axisymmetric form observed in Figure 20. This suggests that for sufficiently high values of λ_z, the post-bifurcation configuration tends toward an axisymmetric bulge.

5. Conclusions

The material model applied in this study may capture the influence of specific parameters associated with the muscle cells that form the arterial wall. Residual stresses are known to play a decisive role in the mechanical behavior of biological structures [73], particularly at arterial bifurcations. Their influence remains the subject of active research and debate [74,75].

The analysis presented here is structured around a three-step mechanical investigation of thick-walled cylindrical tubes. The primary goal is to study bifurcation behavior in tubes subjected to combined axial stretching and internal pressurization. A dis-

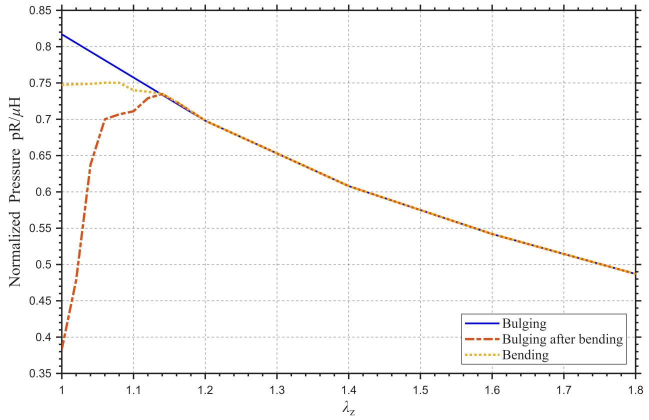

Fig. 17. Normalized inflation pressure at bifurcation against axial stretch for the Case $\bar{\alpha}_d = -15$ and $\bar{\alpha}_c = 0.5$. For sufficiently small values of λ_z, there are three curves: The solid line is for values of pure bulging bifurcation (in a condition of zero azimuthal displacements), then the dash-dotted and dotted lines are the bending bifurcation and the one-sided bulge, respectively, under no restrictions for these displacements. For large values of λ_z after a limit value, the bending mode does not occur.

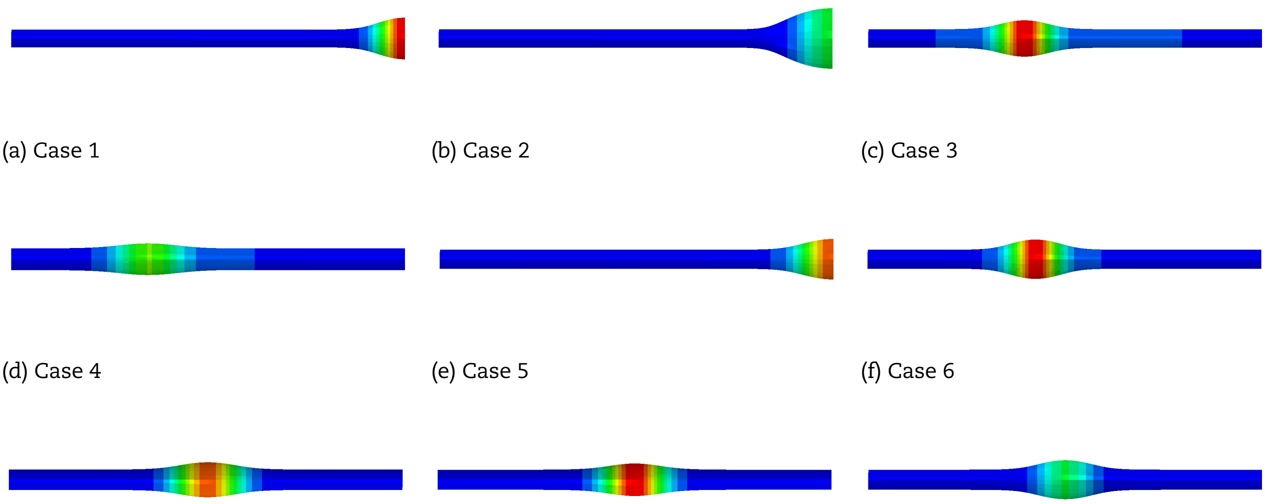

(a) Case 1 (b) Case 2 (c) Case 3

(d) Case 4 (e) Case 5 (f) Case 6

(g) Case 7 (h) Case 8 (i) Case 9

Fig. 18. Post-bifurcations associated with bulging for the combinations of parameters $\bar{\alpha}_d$ and $\bar{\alpha}_c$ that are listed in Table 1, taking an axial stretch of $\lambda_z = 1.6$. The magnitude and the location of the instability vary for different distributions of the residual stresses.

tinguishing feature of this work is the explicit inclusion of a residual stress tensor, defined in three directions in the reference configuration, as the initial condition for the simulations.

Results show that the axial component of this tensor can determine the location of bulging along the tube's length in the post-bifurcation state. The parameters α_d and α_c govern whether the bulge forms near the center or towards the ends of the tube. For small axial stretches, the bifurcation tends to initiate through a bending mode—bending in which subsequently a localized bulge is formed—while higher stretch levels make this bifurcation mode less likely. When examining the normalized bifurcation pressure as a function of the axial stretch λ_z, lower stretch values place the bifurcation firmly within the bending regime, as indicated by the reduced pressure threshold compared to models restricted to develop pure bulging. This finding suggests that, under certain conditions, delaying bifurcation could potentially postpone the onset of aneurysms. Bulging triggered by bending is observed on one side of the tube, a deformation pattern reminiscent of abdominal aortic aneurysms (AAA). Insights from this analysis may therefore contribute to predictive modeling of such pathologies. The bulge location, as predicted by the adopted methodology, is inherently asymmetric.

The study demonstrates the conditions under which the developed finite element model reaches instability during mechanical loading, mimicking the behavior of arterial tissue in critical states arising from physiological activity. Implemented in `Abaqus` via a user-defined material subroutine, the model effectively captures the interplay between non-planar residual stresses and the mechanical response of hyperelastic cylindrical tubes. This provides a practical framework for examining the problem under varying conditions without resorting to overly complex analytical formulations.

It should be noted that the neo-Hookean formulation used here represents an idealization. At large deformations, soft tissues undergo damage and softening [76], both of which strongly influence the onset of instability. Furthermore, arterial walls are typically composed of multiple layers with collagen fibers arranged in distinct orientations [43]. The role of such fiber architectures in triggering bulging has been addressed, for example, in [15,77]. Nonetheless, even in isotropic materials, the initiation of instability

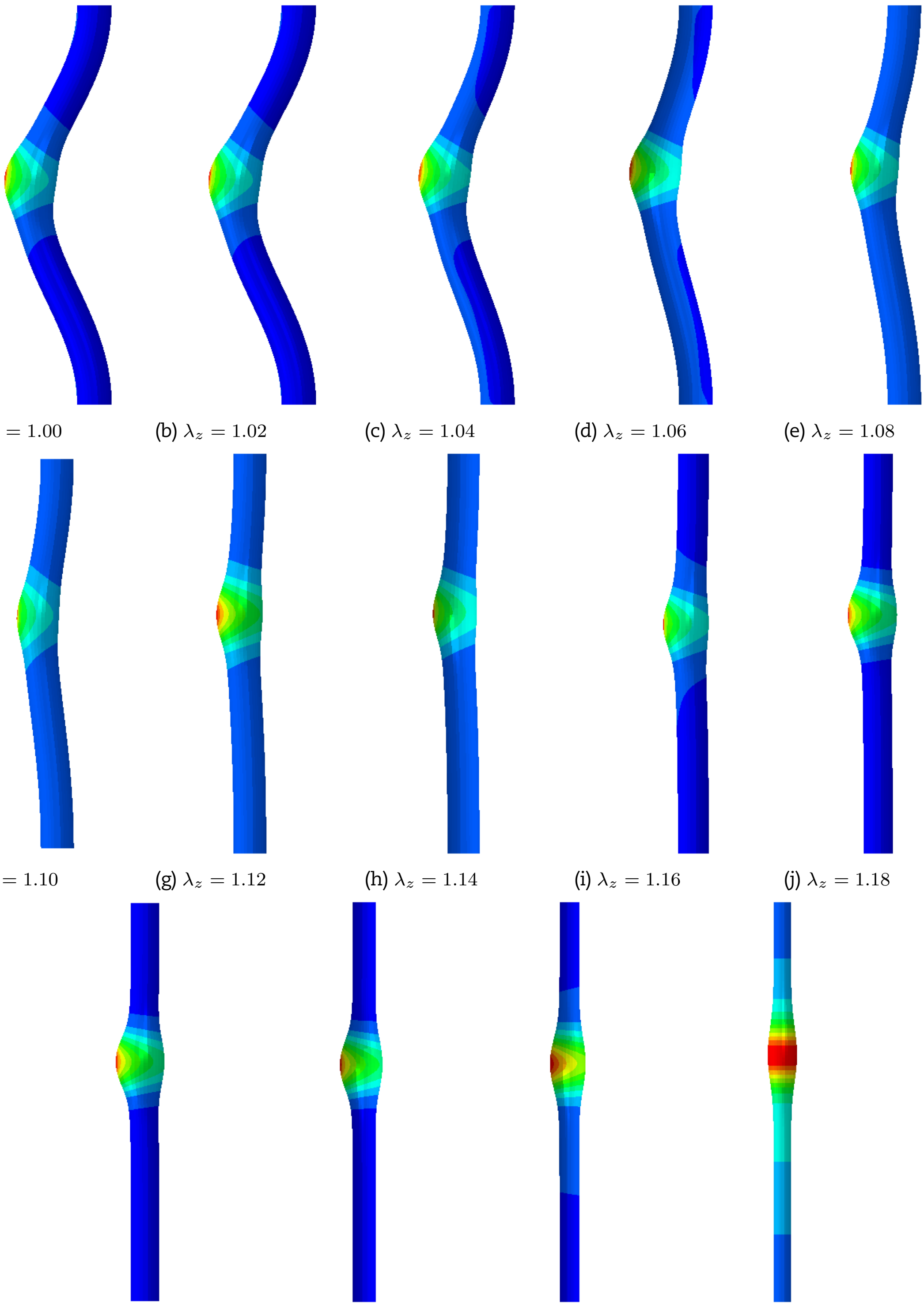

(a) $\lambda_z = 1.00$ (b) $\lambda_z = 1.02$ (c) $\lambda_z = 1.04$ (d) $\lambda_z = 1.06$ (e) $\lambda_z = 1.08$

(f) $\lambda_z = 1.10$ (g) $\lambda_z = 1.12$ (h) $\lambda_z = 1.14$ (i) $\lambda_z = 1.16$ (j) $\lambda_z = 1.18$

(k) $\lambda_z = 1.20$ (l) $\lambda_z = 1.22$ (m) $\lambda_z = 1.24$ (n) $\lambda_z = 1.26$

Fig. 19. Post-bifurcations associated with bending, taking the parameters $\bar{\alpha}_{\rm d} = -15,\ \bar{\alpha}_{\rm c} = 0.5$ (Case 3) for the distribution of the residual stresses. The panels are for different axial stretch values, which correspond to the dash-dotted lines in Fig. 17.

depends on the combined effects of geometry, constitutive behavior, and volumetric changes [49]. Finally, many studies of bifurcation phenomena focus exclusively on elastic responses, overlooking the fact that soft tissue properties evolve as a result of growth, remodeling, and healing [9, 25, 78, 79, 79, 80].

While this study considers a fixed initial cylinder geometry with neo-Hookean material behavior and residual stresses, it is important to note that arterial properties can vary considerably with location in the body, age, sex, and many other factors. Assessing how sensitive the inflation pressure is to changes in geometry, material parameters, constituent arrangement, residual stresses, or other variables—especially when these parameters follow different distributions—requires the use of suitable sensitivity analysis techniques. Such analyses have been carried out by accounting for a wide range of effects, including residual stresses, fiber prestrain, and variations in fiber orientation (see, for example, Asghari et al. [62, 81–84]).

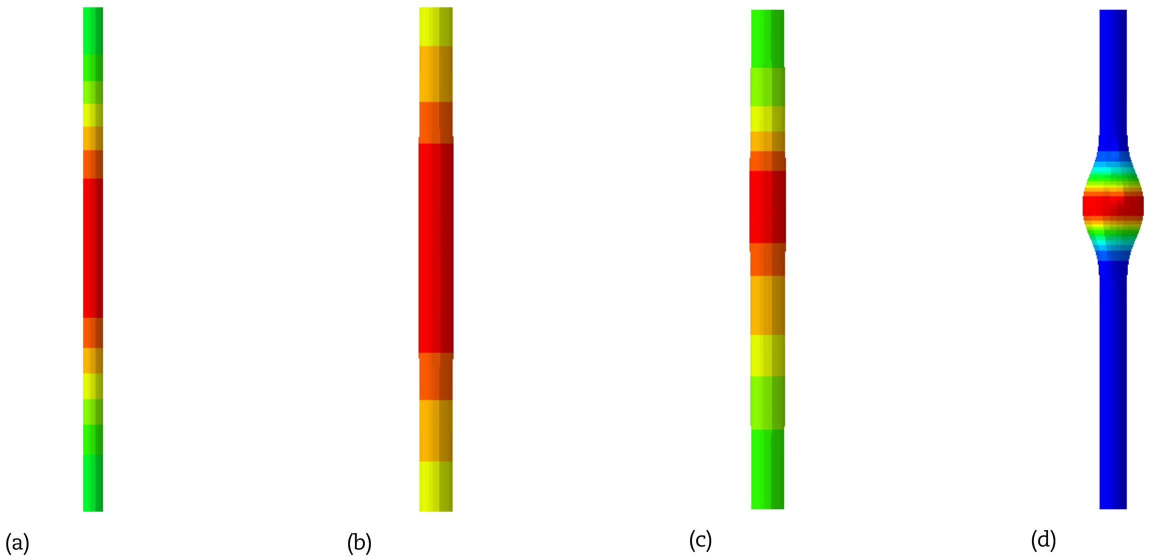

Fig. 20. Illustrated example of the formation history of a bulge, starting from its initiation in panel (a) until the final configuration in panel (d) after its radial propagation, taking the parameters $\bar{\alpha}_{\mathrm{d}} = -15,\ \bar{\alpha}_{\mathrm{c}} = 0.5$ for the residual stresses (Case 3) and an axial stretch of $\lambda_z = 1.40$.

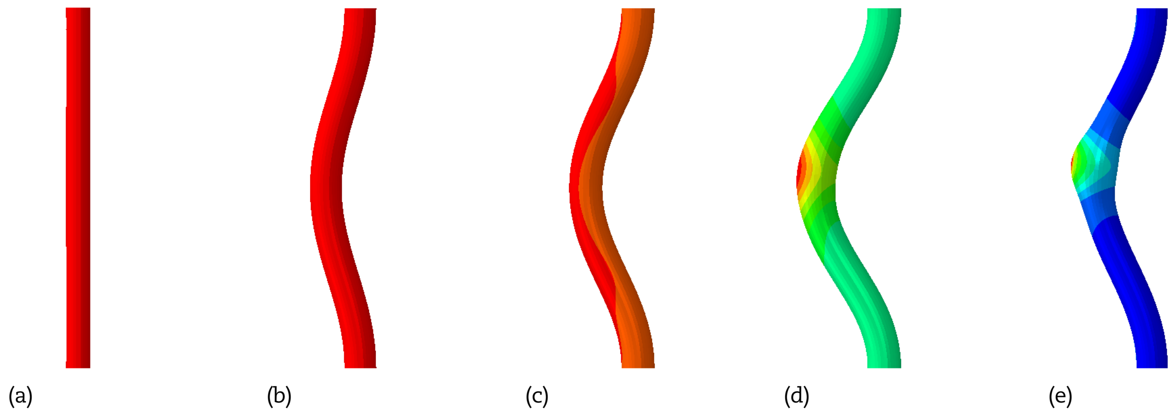

Fig. 21. Illustrated example of the formation history of a bending instability, starting from its initiation in panel (a) until the final configuration in panel (e), taking the parameters $\bar{\alpha}_{\mathrm{d}} = -15,\ \bar{\alpha}_{\mathrm{c}} = 0.5$ for the residual stresses (Case 3) and an axial stretch of $\lambda_z = 1.02$. In the final configuration, one can observe a bulge that has propagated radially.

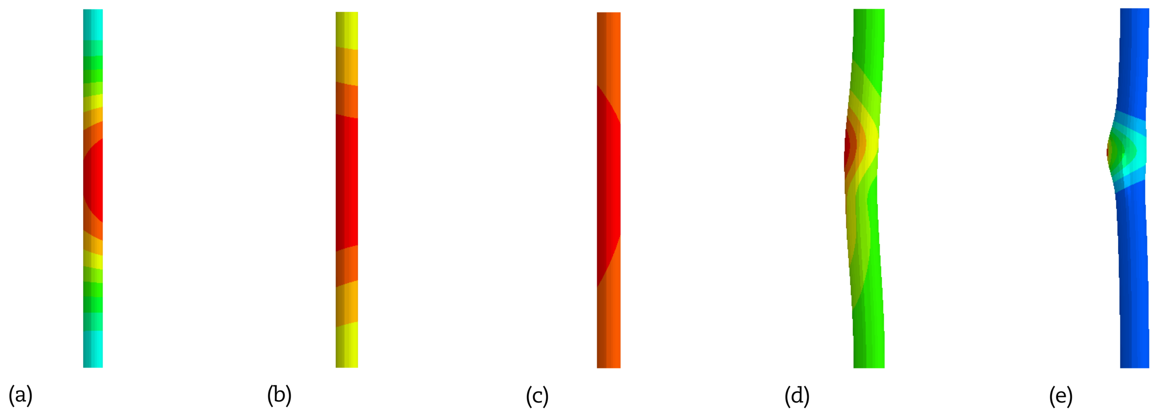

Fig. 22. Illustrated example of the formation history of a bending instability, starting from its initiation in panel (a) until the final configuration in panel (e), taking the parameters $\bar{\alpha}_{\mathrm{d}} = -15,\ \bar{\alpha}_{\mathrm{c}} = 0.5$ for the residual stresses (Case 3) and an axial stretch of $\lambda_z = 1.14$. In the final configuration, one can observe a one-sided bulge that has propagated radially.

Author Contributions

M.J. Al-Chlaihawi and A. Font conducted formal analysis, software programming, the investigation, and the validation and visualization of the results. H. Topol and H. Demirkoparan also conducted the formal analysis, the investigation, and the validation of the results. J. Merodio was involved in the conceptualization, the formal analysis, the investigation of the problem, the supervision of the research process, the validation of the results, and the visualization. All authors were involved in writing the original draft and in the review and editing processes.

Acknowledgments

We thank the reviewers for their valuable comments.

Conflict of Interest

The authors have no relevant financial or non-financial interests to disclose.

Funding

No funding was received for conducting this study.

Data Availability Statements

The datasets generated and/or analyzed during the current study are available from the corresponding author on reasonable request.

References

[1] Lindsay, M., Dietz, H., Lessons on the pathogenesis of aneurysm from heritable conditions, *Nature*, 473, 2011, 308–31.
[2] Schermerhorn, M., A 66-year-old man with an abdominal aortic aneurysm: review of screening and treatment, *JAMA*, 302, 2009, 2015–2022.
[3] Rodríguez, J., Merodio, J., A new derivation of the bifurcation conditions of inflated cylindrical membranes of elastic material under axial loading. application to aneurysm formation, *Mechanics Research Communications*, 38, 2010, 203–210.
[4] Holzapfel, G.A., Ogden, R.W., Biomechanical relevance of the microstructure in artery walls with a focus on passive and active components, *American Journal of Physiology - Heart and Circulatory Physiology*, 315, 2018, H540–H549.
[5] Gonçalves, P.B., Pamplona, D.C., Lopes, S.R.X., Finite deformations of an initially stressed cylindrical shell under internal pressure, *International Journal of Mechanical Sciences*, 50, 2008, 92–103.
[6] Hejazi, M., Hsiang, Y., Phani, A.S., Fate of a bulge in an inflated hyperelastic tube: theory and experiment, *Proceedings of the Royal Society A: Mathematical, Physical and Engineering Sciences*, 477, 2021, 20200837.
[7] Hejazi, M., Phani, A.S., On growth, buckling, and rupture of aneurysms: Cylindrical tube analogy, *Journal of Biomechanics*, 144, 2022, 111313.
[8] Geest, J.P.V., Sacks, M.S., Vorp, D.A., The effects of aneurysm on the biaxial mechanical behavior of human abdominal aorta, *Journal of Biomechanics*, 39, 2006, 1324–1334.
[9] Humphrey, J.D., Mechanisms of arterial remodeling in hypertension: coupled roles of wall shear and intramural stress, *Hypertension*, 52, 2008, 195–200.
[10] Gasser, T.C., Ogden, R.W., Holzapfel, G.A., Hyperelastic modelling of arterial layers with distributed collagen fibre orientations, *Journal of the Royal Society Interface*, 3, 2006, 15–35.
[11] Holzapfel, G.A., Gasser, T.C., Ogden, R.W., A new constitutive framework for arterial wall mechanics and a comparative study of material models, *Journal of Elasticity*, 61, 2000, 1–48.
[12] Taylor, C.A., Figueroa, C.A., Patient-specific modeling of cardiovascular mechanics, *Annual Review of Biomedical Engineering*, 11, 2009, 109–134.
[13] Baek, S., Rajagopal, K.R., Humphrey, J.D., A theoretical model of enlarging intracranial fusiform aneurysms, *Journal of Biomechanical Engineering*, 128, 2006, 142–149.
[14] Al-Chlaihawi, M.J., Topol, H., Demirkoparan, H., Merodio, J., On prismatic and bending bifurcations of fiber reinforced elastic membranes under swelling with application to aortic aneurysms, *Mathematics and Mechanics of Solids*, 28, 2023, 108–123.
[15] Topol, H., Al-Chlaihawi, M.J., Demirkoparan, H., Merodio, J., Bulging initiation and propagation in fiber-reinforced swellable Mooney-Rivlin membranes, *Journal of Engineering Mathematics*, 128, 2021, 8.
[16] Topol, H., Al-Chlaihawi, M.J., Demirkoparan, H., Merodio, J., Bifurcation of fiber-reinforced cylindrical membranes under extension, inflation, and swelling, *Journal of Applied and Computational Mechanics*, 9, 2023, 113–128.
[17] Alhayani, A.A., Giraldo, J.A., Rodriguez, J., Merodio, J., Computational modelling of bulging of inflated cylindrical shell applicable to aneurysm formation and propagation in arterial wall tissue, *Finite Elements in Analysis and Design*, 73, 2013, 20–29.
[18] Alhayani, A.A., Rodriguez, J., Merodio, J., Competition between radial expansion and axial propagation in bulging of inflated cylinders with application to aneurysms propagation in arterial wall tissue, *International Journal of Engineering Science*, 85, 2014, 74–89.
[19] Dehghani, H., Desena-Galarza, D., Jha, N.K., Reinoso, J., Merodio, J., Bifurcation and post-bifurcation of an inflated and extended residually-stressed circular cylindrical tube with application to aneurysms initiation and propagation in arterial wall tissue, *Finite Elements in Analysis and Design*, 161, 2019, 51–60.
[20] Font, A., Jha, N.K., Dehghani, H., Reinoso, J., Merodio, J., Modelling of residually stressed, extended and inflated cylinders with application to aneurysms, *Mechanics Research Communications*, 111, 2021, 103643.
[21] Fu, Y., Rogerson, G., Zhang, Y., Initiation of aneurysms as a mechanical bifurcation phenomenon, *International Journal of Non-Linear Mechanics*, 47, 2012, 179–184.
[22] Merodio, J., Haughton, D., Bifurcation of thick-walled cylinder shells and the mechanical response of arterial tissue affected by Marfan's syndrome, *Mechanics Research Communications*, 38, 2010, 1–6.
[23] Al-Chlaihawi, M.J., Desena-Galarza, D., Topol, H., Merodio, J., Computational modeling of a residually stressed thick-walled cylinder under the combined action of axial extension and inflation, *Finite Elements in Analysis and Design*, 244, 2025, 104309.
[24] Saini, K., Cho, S., Dooling, L.J., Discher, D.E., Tension in fibrils suppresses their enzymatic degradation - a molecular mechanism for 'use it or lose it', *Matrix Biology*, 85-86, 2020, 34–46.
[25] Topol, H., Demirkoparan, H., Pence, T.J., Fibrillar collagen: A review of the mechanical modeling of strain-mediated enzymatic turnover, *Applied Mechanics Reviews*, 73, 2021, 050802.
[26] Tonge, T.K., Ruberti, J.W., Nguyen, T.D., Micromechanical modeling study of mechanical inhibition of enzymatic degradation of collagen tissues, *Biophysical Journal*, 109, 2015, 2689–2700.
[27] Vangerko, H., Treloar, L.R.G., The inflation and extension of rubber tube for biaxial strain studies, *Journal of Physics D: Applied Physics*, 11, 1978, 1969.
[28] Kyriakides, S., Chang, Y.C., On the inflation of a long elastic tube in the presence of axial load, *International Journal of Solids and Structures*, 26, 1990, 975–991.
[29] Kyriakides, S., Yu-Chung, C., The initiation and propagation of a localized instability in an inflated elastic tube, *International Journal of Solids and Structures*, 27, 1991, 1085–1111.
[30] Wang, S., Guo, Z., Zhou, L., Li, L., Fu, Y., An experimental study of localized bulging in inflated cylindrical tubes guided by newly emerged analytical results, *Journal of the Mechanics and Physics of Solids*, 124, 2019, 536–554.
[31] Haughton, D.M., Ogden, R.W., Bifurcation of inflated circular cylinders of elastic material under axial loading - I. Membrane theory for thin-walled tubes, *Journal of the Mechanics and Physics of Solids*, 27, 1979, 179–212.
[32] Haughton, D., Ogden, R., Bifurcation of inflated circular cylinders of elastic material under axial loading-II. Exact theory for thick-walled tubes, *Journal of the Mechanics and Physics of Solids*, 27, 1979, 489–512.

[33] Haseganu, E.M., Steigmann, D.J., Theoretical flexural response of a pressurized cylindrical membrane, *International Journal of Solids and Structures*, 31, 1994, 27–50.
[34] Fu, Y.B., Pearce, S.P., Liu, K.K., Post-bifurcation analysis of a thin-walled hyperelastic tube under inflation, *International Journal of Non-Linear Mechanics*, 43, 2008, 697–706.
[35] Fu, Y.B., Xie, Y.X., Effects of imperfections on localized bulging in inflated membrane tubes, *Philosophical Transactions of the Royal Society A: Mathematical, Physical and Engineering Sciences*, 370, 2012, 1896–1911.
[36] Desena-Galarza, D., Dehghani, H., Jha, N.K., Reinoso, J., Merodio, J., Computational bifurcation analysis for hyperelastic residually stressed tubes under combined inflation and extension and aneurysms in arterial tissue, *Finite Elements in Analysis and Design*, 197, 2021, 103636.
[37] Desena Galarza, D., *Computational modelling of hyperelastic incompressible residually stressed cylindrical tubes with application to instabilities in arterial tissues*, Universidad Politécnica de Madrid, 2025.
[38] Hoger, A., On the determination of residual stress in an elastic body, *Journal of Elasticity*, 16, 1986, 303–324.
[39] Hoger, A., Residual stress in an elastic body: a theory for small strains and arbitrary rotations, *Journal of Elasticity*, 31, 1993, 1–24.
[40] Nam, N.T., Merodio, J., Ogden, R.W., Vinh, P.C., The effect of initial stress on the propagation of surface waves in a layered half-space, *International Journal of Solids and Structures*, 88, 2016, 88–100.
[41] Merodio, J., Ogden, R.W., Rodríguez, J., The influence of residual stress on finite deformation elastic response, *International Journal of Non-Linear Mechanics*, 56, 2013, 43–49.
[42] Merodio, J., Ogden, R.W., Extension, inflation, and torsion of a residually stressed circular cylindrical tube, *Continuum Mechanics and Thermodynamics*, 28, 2016, 157–174.
[43] Holzapfel, G.A., Ogden, R.W., Modelling the layer-specific three-dimensional residual stresses in arteries, with an application to the human aorta, *Journal of the Royal Society Interface*, 7, 2010, 787–799.
[44] Ahamed, T., Dorfmann, L., Ogden, R.W., Modelling of residually stressed materials with application to AAA, *Journal of the Mechanical Behavior of Biomedical Materials*, 61, 2016, 221–234.
[45] Simulia., Abaqus analysis user's guide, version 6.14, 2014.
[46] O'Leary, D.H., Polak, J.F., Intima-media thickness: A tool for atherosclerosis imaging and event prediction, *American Journal of Cardiology*, 90, 2002, L18–L21.
[47] Polak, J.F., Pencina, M.J., Meisner, A., Pencina, K.M., Brown, L.S., Wolf, P.A., D'Agostino Sr, R.B., Associations of carotid artery intima-media thickness (IMT) with risk factors and prevalent cardiovascular disease, *Journal of Ultrasound in Medicine*, 29, 2010, 1759–1768.
[48] Gou, K., Topol, H., Demirkopraran, H., Pence, T.J., Stress-swelling finite element modeling of cervical response with homeostatic collagen fiber distributions, *Journal of Biomechanical Engineering*, 142, 2020, 081002.
[49] Moradalizadeh, S., Topol, H., Demirkoparan, H., Melnikov, A., Markert, B., Merodio, J., Remarks on bifurcation of an inflated and extended swellable isotropic tube, *Mathematics and Mechanics of Solids*, 29, 2024, 474–493.
[50] Nazari, H., Topol, H., Demirkoparan, H., Ghandvar, H., Merodio, J., Material volume changes in residually stressed idealized arteries, *European Journal of Mechanics - A/Solids*, 112, 2025, 105676.
[51] Topol, H., Demirkoparan, H., Pence, T.J., Wineman, A., Time-evolving collagen-like structural fibers in soft tissues: Biaxial loading and spherical inflation, *Mechanics of Time-Dependent Materials*, 21, 2017, 1–29.
[52] Topol, H., Demirkoparan, H., Pence, T.J., Wineman, A., Uniaxial load analysis under stretch-dependent fiber remodeling applicable to collagenous tissue, *Journal of Engineering Mathematics*, 95, 2015, 325–345.
[53] Bustamante, R., Holzapfel, G., Methods to compute 3D residual stress distributions in hyperelastic tubes with application to arterial walls, *International Journal of Engineering Science*, 48, 2010, 1066–1082.
[54] Waffenschmidt, T., Menzel, A., Extremal states of energy of a double-layered thick-walled tube – application to residually stressed arteries, *Journal of the Mechanical Behavior of Biomedical Materials*, 29, 2014, 635–654.
[55] Sigaeva, T., Sommer, G., Holzapfel, G.A., Di Martino, E.S., Anisotropic residual stresses in arteries, *Journal of the Royal Society Interface*, 16, 2019, 20190029.
[56] Li, B., Roper, S.M., Wang, L., Luo, X., Hill, N.A., An incremental deformation model of arterial dissection, *Journal of Mathematical Biology*, 78, 2019, 1277–1298.
[57] Zhuan, X., Luo, X., Residual stress estimates from multi-cut opening angles of the left ventricle, *Cardiovascular Engineering and Technology*, 11, 2020, 381–393.
[58] Melnikov, A., Ogden, R.W., Dorfmann, L., Merodio, J., Bifurcation analysis of elastic residually-stressed circular cylindrical tubes, *International Journal of Solids and Structures*, 226-227, 2021, 111062.
[59] Melnikov, A., Merodio, J., Bustamante, R., Dorfmann, L., Bifurcation analysis of residually stressed neo-Hookean and Ogden electroelastic tubes, *Philosophical Transactions of the Royal Society A: Mathematical, Physical and Engineering Sciences*, 380, 2022, 20210331.
[60] Melnikov, A., Merodio, J., Stability analysis of an inflated, axially extended, residually stressed circular cylindrical tube, *Journal of Applied and Computational Mechanics*, 9(3), 2023, 834–847.
[61] Moradalizadeh, S., Nazari, H., Topol, H., Merodio, J., Bulging bifurcation in residually stressed cylindrical double-layered thick-walled cylinders applicable to the modeling of arteries, *Journal of Applied and Computational Mechanics*, 11, 2025, 1060–1074.
[62] Asghari, H., Topol, H., Markert, B., Merodio, J., Application of the extended fourier amplitude sensitivity testing (FAST) method to inflated, axial stretched, and residually stressed cylinders, *Applied Mathematics and Mechanics (English Edition)*, 44, 2023, 2139–2162.
[63] Gundiah, N., Ratcliffe, M.B., Pruitt, L.A., Determination of strain energy function for arterial elastin: Experiments using histology and mechanical tests, *Journal of Biomechanics*, 40, 2007, 586–594.
[64] Merodio, J., Ogden, R., *Constitutive Theory of Nonlinear Elasticity*, Springer Nature Switzerland, Cham, 17–53, 2025.
[65] Tutino, V.M., Rajabzadeh-Oghaz, H., Veeturi, S.S., Poppenberg, K.E., Waqas, M., Mandelbaum, M., Liaw, N., Siddiqui, A.H., Meng, H., Kolega, J., Endogenous animal models of intracranial aneurysm development: a review, *Neurosurgical Review*, 44, 2021, 2545–2570.
[66] Guo, Z., Wang, S., Fu, Y., Localized bulging of an inflated rubber tube with fixed ends, *Philosophical Transactions of the Royal Society A: Mathematical, Physical and Engineering Sciences*, 380, 2022, 20210318.
[67] Hayreh, S.S., Servais, G.R., Virdi, P.S., Retinal arteriolar changes in malignant arterial hypertension, *Ophthalmologica*, 198, 2010, 178–196.
[68] Taarnhøj, N.C.B.B., Munch, I.C., Sander, B., Kessel, L., Hougaard, J.L., Kyvik, K., Sørensen, T.I.A., Larsen, M., Straight versus tortuous retinal arteries in relation to blood pressure and genetics, *British Journal of Ophthalmology*, 92, 2008, 1055–1060.
[69] Jackson, Z.S., Dajnowiec, D., Gotlieb, A.I., Langille, B.L., Partial off-loading of longitudinal tension induces arterial tortuosity, *Arteriosclerosis, Thrombosis, and Vascular Biology*, 25, 2005, 957–962.
[70] Fortier, A., Gullapalli, V., Mirshams, R.A., Review of biomechanical studies of arteries and their effect on stent performance, *IJC Heart & Vasculature*, 4, 2014, 12–18.
[71] Rodríguez, J., Merodio, J., Helical buckling and postbuckling of pre-stressed cylindrical tubes under finite torsion, *Finite Elements in Analysis and Design*, 112, 2016, 1–10.
[72] Ye, Y., Liu, Y., Althobaiti, A., Xie, Y.X., Localized bulging in an inflated bilayer tube of arbitrary thickness: Effects of the stiffness ratio and constitutive model, *International Journal of Solids and Structures*, 176-177, 2019, 173–184.
[73] Liu, S.Q., Fung, Y.C., Zero-stress states of arteries, *Journal of Biomechanical Engineering*, 110, 1988, 82–84.
[74] Laubrie, J.D., Mousavi, J.S., Avril, S., A new finite-element shell model for arterial growth and remodeling after stent implantation, *International Journal for Numerical Methods in Biomedical Engineering*, 36, 2020, e3282.
[75] Giudici, A., Wilkinson, I.B., Khir, A.W., Review of the techniques used for investigating the role elastin and collagen play in arterial wall mechanics, *IEEE Reviews in Biomedical Engineering*, 14, 2020, 256–269.
[76] Holzapfel, G.A., Ogden, R.W., A damage model for collagen fibres with an application to collagenous soft tissues, *Proceedings of the Royal Society A: Mathematical, Physical and Engineering Sciences*, 476, 2020, 20190821.
[77] Topol, H., Asghari, H., Stoffel, M., Markert, B., Merodio, J., Post-bifurcation of inflated fibrous cylindrical membranes under different fiber configurations, *European Journal of Mechanics - A/Solids*, 101, 2023, 105065.
[78] Gierig, M., Wriggers, P., Marino, M., Computational model of damage-induced growth in soft biological tissues considering the mechanobiology of healing, *Biomechanics and Modeling in Mechanobiology*, 20, 2021, 1297–1315.

[79] Topol, H., Pence, T.J., Homeostatic collagen remodeling: enzymatic strain stabilization and large strain softening in pressurized thick-walled cylindrical vessels, *Mechanics of Soft Materials*, 6, 7.
[80] Topol, H., Demirkoparan, H., Pence, T.J., Modeling stretch-dependent collagen fiber density, *Mechanics Research Communications*, 116, 2021, 103740.
[81] Asghari, H., Topol, H., Lacalle, J., Merodio, J., Sensitivity analysis of an inflated and extended fiber-reinforced membrane with different natural configurations of its constituents, *Mathematics and Mechanics of Solids*, 30, 2025, 942–978.
[82] Asghari, H., Topol, H., Lacalle, J., Merodio, J., Sensitivity analysis of fibrous thick-walled tubes with mechano-sensitive remodeling fibers in homeostasis, *Acta Mechanica*, 235, 2024, 5727–5745.
[83] Asghari, H., Topol, H., Markert, B., Merodio, J., Application of sensitivity analysis in extension, inflation, and torsion of residually stressed circular cylindrical tubes, *Probabilistic Engineering Mechanics*, 73, 2023, 103469.
[84] Asghari, H., Topol, H., Melnikov, A., Spitas, C., Merodio, J., Inflation and extension of soft fibrous membranes that account for fiber dispersion and pre-stretch: a sensitivity analysis, *Mathematics and Mechanics of Solids*, accepted in June 2025.

ORCID iD

Murtadha J. Al-Chlaihawi https://orcid.org/0000-0003-2036-3231
Alejandro Font https://orcid.org/0009-0006-3888-1693
Heiko Topol https://orcid.org/0000-0002-4845-7515
Hasan Demirkoparan https://orcid.org/0000-0003-1713-0349
José Merodio https://orcid.org/0000-0001-5602-4659

How to cite this article: Murtadha J. Al-Chlaihawi, Alejandro Font, Heiko Topol, Hasan Demirkoparan, José Merodio. Bulging and Bending of a Thick-Walled Cylinder with Residual Stress under Combined Extension and Inflation, J. Appl. Comput. Mech., 12(3), 2026, 1256-1275. https://doi.org/10.22055/jacm.2026.48955.5622